

# 1 Predicting resistance of clinical Abl 2 mutations to targeted kinase inhibitors 3 using alchemical free-energy 4 calculations

5 **Kevin Hauser<sup>1</sup>, Christopher Negron<sup>1</sup>, Steven K. Albanese<sup>2,3</sup>, Soumya Ray<sup>1</sup>, Thomas  
6 Steinbrecher<sup>4</sup>, Robert Abel<sup>1</sup>, John D. Chodera<sup>3</sup>, Lingle Wang<sup>1\*</sup>**

7 <sup>1</sup>Schrödinger, New York, NY 10036; <sup>2</sup>Gerstner Sloan Kettering Graduate School, Memorial Sloan  
8 Kettering Cancer Center, New York, NY 10065; <sup>3</sup>Computational and Systems Biology Program,  
9 Sloan Kettering Institute, Memorial Sloan Kettering Cancer Center, New York, NY 10065;  
10 <sup>4</sup>Schrödinger, GmbH, Q7 23, 68161 Mannheim, Germany

11 **\*For correspondence:** [lingle.wang@schrodinger.com](mailto:lingle.wang@schrodinger.com) (LW)

13 **Abstract** The therapeutic effect of targeted kinase inhibitors can be significantly reduced by intrinsic or  
14 acquired resistance mutations that modulate the affinity of the drug for the kinase. In cancer, the majority of  
15 missense mutations are rare, making it difficult to predict their impact on inhibitor affinity. This complicates  
16 the practice of precision medicine, pairing of patients with clinical trials, and development of next-generation  
17 inhibitors. Here, we examine the potential for alchemical free-energy calculations to predict how kinase  
18 mutations modulate inhibitor affinities to Abl, a major target in chronic myelogenous leukemia (CML). We  
19 find these calculations can achieve useful accuracy in predicting resistance for a set of eight FDA-approved  
20 kinase inhibitors across 144 clinically-identified point mutations, achieving a root mean square error in  
21 binding free energy changes of  $1.1_{-0.9}^{+1.3}$  kcal/mol (95% confidence interval) and correctly classifying mutations  
22 as resistant or susceptible with 88<sup>93</sup><sub>82</sub>% accuracy. Since these calculations are fast on modern GPUs, this  
23 benchmark establishes the potential for physical modeling to collaboratively support the rapid assessment  
24 and anticipation of the potential for patient mutations to affect drug potency in clinical applications.

25  
26 Targeted kinase inhibitors are a major therapeutic class in the treatment of cancer. A total of 38 selective  
27 small molecule kinase inhibitors have now been approved by the FDA [1], including 34 approved to treat  
28 cancer, and perhaps 50% of all current drugs in development target kinases [2]. Despite the success of  
29 selective inhibitors, the emergence of drug resistance remains a challenge in the treatment of cancer [3–10]  
30 and has motivated the development of second- and then third-generation inhibitors aimed at overcoming  
31 recurrent resistance mutations [11–15].

32 While a number of drug resistance mechanisms have been identified in cancer (e.g., induction of splice  
33 variants [16], or alleviation of feedback [17]), inherent or acquired missense mutations in the kinase domain  
34 of the target of therapy are a major form of resistance to tyrosine kinase inhibitors (TKI) [10, 18, 19]. Oncology  
35 is entering a new era with major cancer centers now deep sequencing tumors to reveal genetic alterations  
36 that may render subclonal populations susceptible or resistant to targeted inhibitors [20], but the use of  
37 this information in precision medicine has lagged behind. It would be of enormous value in clinical practice  
38 if an oncologist could reliably ascertain whether these mutations render the target of therapy resistant or  
39 susceptible to available inhibitors; such tools would facilitate the enrollment of patients in mechanism-based

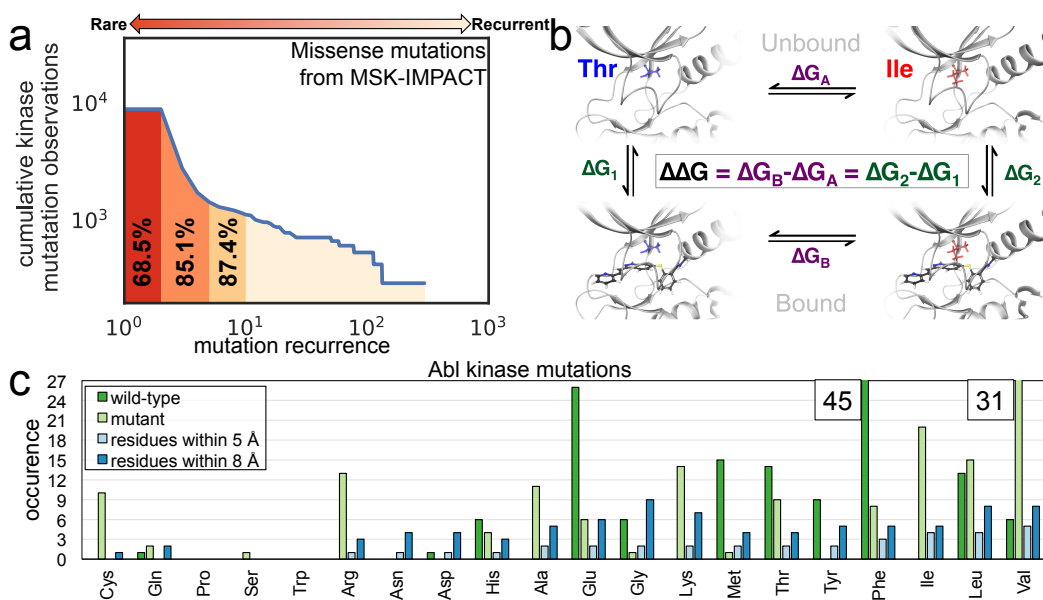


**Figure 1. Relative alchemical free-energy calculations can be used to predict affinity changes of FDA-approved selective kinase inhibitors arising from clinically-identified mutations in their targets of therapy.** (a) Missense mutation statistics derived from 10,336 patient samples subjected to MSK-IMPACT deep sequencing panel [20] show that 68.5% of missense kinase mutations in cancer patients have never been observed previously, while 87.4% have been observed no more than ten times. (b) To compute the impact of a clinical point mutation on inhibitor binding free energy, a thermodynamic cycle can be used to relate the free energy of the wild-type and mutant kinase in the absence (top) and presence (bottom) of the inhibitor. (c) Summary of mutations studied in this work. Frequency of the wild-type (dark green) and mutant (green) residues for the 144 clinically-identified Abl mutations used in this study (see *Table 1* for data sources). Also shown is the frequency of residues within 5 Å (light blue) and 8 Å (blue) of the binding pocket. The number of wild-type Phe residues (n=45) and mutant Val residues (n=31) exceeded the limits of the y-axis.

40 basket trials [21, 22], help prioritize candidate compounds for clinical trials, and aid the development of  
41 next-generation inhibitors.

42 The long tail of rare kinase mutations frustrates prediction of drug resistance  
43 While some cancer missense mutations are highly recurrent and have been characterized clinically or  
44 biochemically, a “long tail” of rare mutations collectively accounts for the majority of clinically observed  
45 missense mutations (*Figure 1a*), leaving clinicians and researchers without knowledge of whether these  
46 uncharacterized mutations might lead to resistance. While rules-based and machine learning schemes  
47 are still being assessed in oncology contexts, work in predicting drug response to microbial resistance has  
48 shown that rare mutations present a significant challenge to approaches that seek to predict resistance  
49 to therapy [23]. Clinical cancer mutations may impact drug response through a variety of mechanisms  
50 by altering kinase activity, ATP affinity, substrate specificities, and the ability to participate in regulatory  
51 interactions, compounding the difficulties associated with limited datasets that machine learning approaches  
52 face. In parallel with computational approaches, high-throughput experimental techniques such as MITE-  
53 Seq [24] have been developed to assess the impact of point mutations on drug response. However, the  
54 complexity of defining selection schemes that reliably correlate with *in vivo* drug effectiveness and long  
55 turn-around times might limit their ability to rapidly and reliably impact clinical decision-making.

56 Alchemical free-energy methods can predict inhibitor binding affinities  
57 Physics-based approaches could be complementary to machine-learning and experimental techniques  
58 in predicting changes in TKI affinity due to mutations with few or no prior clinical observations. Modern  
59 atomistic molecular mechanics forcefields such as OPLS3 [25], CHARMM [26], and AMBER FF14SB [27] have  
60 reached a sufficient level of maturity to enable the accurate and reliable prediction of receptor-ligand binding  
61 free energy. Alchemical free-energy methods permit receptor-ligand binding energies to be computed

62 rigorously, including all relevant entropic and enthalpic contributions [28]. Encouragingly, kinase:inhibitor  
63 binding affinities have been predicted using alchemical free-energy methods with mean unsigned errors of  
64 1.0 kcal/mol for CDK2, JNK1, p38, and Tyk2 [29, 30]. Beyond kinases, alchemical approaches have predicted  
65 the binding affinity of BRD4 inhibitors with mean absolute errors of 0.6 kcal/mol [31]. Alchemical methods  
66 have also been observed to have good accuracy (0.6 kcal/mol mean unsigned error for Tyk2 tyrosine kinase)  
67 in the prediction of relative free energies for ligand transformations within a complex whose receptor  
68 geometry was generated using a homology model [32].

69 Alchemical approaches can predict the impact of protein mutations on free energy  
70 Alchemical free-energy calculations have also been used to predict the impact of mutations on protein-  
71 protein binding [33] and protein thermostabilities [34]. Recent work has found that protein mutations can  
72 be predicted to be stabilizing or destabilizing with a classification accuracy of 71% across ten proteins and 62  
73 mutations [35]. The impact of Gly to D-Ala mutations on protein stability was predicted using an alchemical  
74 approach with a similar level of accuracy [36]. Recently, one study has hinted at the potential utility of  
75 alchemical free-energy calculations in oncology by predicting the impact of a single clinical mutation on the  
76 binding free energies of the TKIs dasatinib and RL45 [37].

77 Assessing the potential for physical modeling to predict resistance to FDA-approved TKIs  
78 Here, we ask whether physical modeling techniques may be useful in predicting whether clinically-identified  
79 kinase mutations lead to drug resistance or drug sensitivity. We perform state-of-the-art relative alchemical  
80 free-energy calculations using FEP+ [29], recently demonstrated to achieve sufficiently good accuracy to drive  
81 the design of small-molecule inhibitors for a broad range of targets during lead optimization [28–30, 38]. We  
82 compare this approach against a fast but approximate physical modeling method implemented in Prime [39]  
83 (an MM-GBSA approach) in which an implicit solvent model is used to assess the change in minimized  
84 interaction energy of the ligand with the mutant and wild-type kinase. We consider whether these methods  
85 can predict a ten-fold reduction in inhibitor affinity (corresponding to a binding free energy change of 1.36  
86 kcal/mol) to assess baseline utility. As a benchmark, we compile a set of reliable inhibitor  $\Delta\text{pIC}_{50}$  data for 144  
87 clinically-identified mutants of the human kinase Abl, an important oncology target dysregulated in cancers  
88 like chronic myelogenous leukemia (CML), for which six [1] FDA-approved TKIs are available. While  $\Delta\text{pIC}_{50}$   
89 can approximate a dissociation constant  $\Delta K_D$ , other processes contributing to changes in cell viability might  
90 affect  $\text{IC}_{50}$  in ways that are not accounted for by a traditional binding experiment, motivating a quantitative  
91 comparison between  $\Delta\text{pIC}_{50}$  and  $\Delta K_D$ . The results of this benchmark demonstrate the potential for FEP+ to  
92 predict the impact that mutations in Abl kinase have on drug binding, and a classification accuracy of 88<sup>93%</sup><sub>82%</sub>  
93 (for all statistical metrics reported in this paper, the 95% confidence intervals (CI) is shown in the form of  
94 ( $x_{\text{lower}}^{\text{upper}}$ )), an RMSE of 1.07<sup>1.26</sup><sub>0.89</sub> kcal/mol, and an MUE of 0.79<sup>0.92</sup><sub>0.67</sub> kcal/mol was achieved.

## 95 Results

96 Free energy calculations can recapitulate the impact of clinical mutations on TKI affinity  
97 Alchemical free-energy calculations utilize a physics-based approach to estimate the free energy of transform-  
98 ing one chemical species into another, incorporating all enthalpic and entropic contributions in a physically  
99 consistent manner [28, 40–42]. While relative alchemical free-energy calculations have typically been em-  
100 ployed in optimizing small molecules for increased potency or selectivity [29, 38, 42, 43], a complementary  
101 alchemical approach can be used to compute the impact of point mutations on ligand binding affinities.  
102 **Figure 1b** depicts the thermodynamic cycle that illustrates how we used relative free energy calculations to  
103 compute the change in ligand binding free energy in response to the introduction of a point mutation in the  
104 kinase. In the *bound* leg of the cycle, the wild-type protein:ligand complex is transformed into the mutant  
105 protein:ligand complex. In the *unbound* leg of the cycle, the *apo* protein is transformed from wild-type into  
106 mutant. To achieve reliable predictions with short relative free-energy calculations, a reliable receptor:ligand  
107 complex structure is required with the assumption that the binding mode of wild-type and mutant are  
108 similar. In this work, high-resolution co-crystal structures of wild-type Abl bound to an inhibitor were utilized  
109 when available. To assess the potential for using docked inhibitor poses, we also examined two systems for

**Table 1. Public  $\Delta\text{pIC}_{50}$  datasets for 144 Abl kinase mutations and eight tyrosine kinase inhibitors (TKIs) with corresponding wild-type co-crystal structures used in this study.**

TKI	$N_{\text{mut}}$	R	S	PDB	(kcal/mol)		$\Delta G_{\text{WT}}$
					$ \Delta G_{\text{max}} - \Delta G_{\text{min}} $	Source	
axitinib	26	0	26	4wa9	2.05	[44]	-8.35
bosutinib	21	4	17	3ue4	2.79	[45]	-9.81
dasatinib	21	5	16	4xey	5.08	[45]	-11.94
imatinib	21	5	16	1opj	2.16	[45]	-9.19
nilotinib	21	4	17	3cs9	3.88	[45]	-10.74
ponatinib	21	0	21	3oxz	1.00	[45]	-11.70
<b>subtotal</b>	<b>131</b>	<b>18</b>	<b>113</b>				
erlotinib	7	1	6	<i>Dock to 3ue4</i>	1.73	[46]	-9.77
gefitinib	6	0	6	<i>Dock to 3ue4</i>	1.79	[46]	-8.84
<b>total</b>	<b>144</b>	<b>19</b>	<b>125</b>				

$N_{\text{mut}}$ : Total number of mutants for which  $\Delta\text{pIC}_{50}$  data was available.

Number of Resistant, Susceptible mutants using 10-fold affinity change threshold.

PDB: Source PDB ID, or *Dock to 3ue4*, which used 3ue4 as the receptor for Glide-SP docking inhibitors without co-crystal structure.

$\Delta G_{\text{WT}}$ : Binding free energy of inhibitor to wild-type Abl, as estimated from  $\text{IC}_{50}$  data.

110 which co-crystal structures were not available (Abl:erlotinib and Abl:gefitinib) and used docking to generate  
111 initial coordinates.

112 Compiled  $\Delta\text{pIC}_{50}$  data provides a benchmark for predicting mutational resistance  
113 To construct a benchmark evaluation dataset, we compiled a total of 144  $\Delta\text{pIC}_{50}$  measurements of Abl:TKI  
114 affinities, summarized in **Table 1**, taking care to ensure all measurements for an individual TKI were reported  
115 in the same study from experiments run under identical conditions. 131  $\Delta\text{pIC}_{50}$  measurements were available  
116 across the six TKIs with available co-crystal structures with wild-type Abl—26 for axitinib and 21 for bosutinib,  
117 dasatinib, imatinib, nilotinib, and ponatinib. 13  $\Delta\text{pIC}_{50}$  measurements were available for the two TKIs for  
118 which docking was necessary to generate Abl:TKI structures—7 for erlotinib and 6 for gefitinib. For added  
119 diversity, this set includes TKIs for which Abl is not the primary target—axitinib, erlotinib, and gefitinib. All  
120 mutations in this benchmark dataset have been clinically-observed (**Table S1**). Due to the change in bond  
121 topology required by mutations involving proline, which is not currently supported by the FEP+ technology for  
122 protein residue mutations, the three mutations H396P (axitinib, gefitinib, erlotinib) were excluded from our  
123 assessment. As single point mutations were highly represented in the IMPACT study analyzed in **Figure 1a**,  
124 we excluded double mutations from this work. However, the impact of mutations from multiple sites can  
125 potentially be modeled by sequentially mutating each site and this will be addressed in future work.

126 Experimental  $\Delta\text{pIC}_{50}$  measurements for wild-type and mutant Abl were converted to  $\Delta\Delta G$  in order  
127 to make direct comparisons between physics-based models and experiment. However, computation  
128 of experimental uncertainties were required to understand the degree to which differences between  
129 predictions and experimental data were significant. Since experimental error estimates for measured  $\text{IC}_{50}$ s  
130 were not available for the data in **Table 1**, we compared that data to other sources that have published  
131  $\text{IC}_{50}$ s for the same mutations in the presence of the same TKIs (**Figure 2a,b,c**). Cross-comparison of 97  
132 experimentally measured  $\Delta\Delta G$ s derived from cell viability assay  $\text{IC}_{50}$  data led to an estimate of experimental  
133 variability of  $0.32^{0.36}_{0.28}$  kcal/mol root-mean square error (RMSE) that described the expected repeatability of the  
134 measurements. Because multiple factors influence the  $\text{IC}_{50}$  aside from direct effects on the binding affinity—  
135 the focus of this study—we also compared  $\Delta\Delta G$ s derived from  $\Delta\text{pIC}_{50}$ s with those derived from binding  
136 affinity measurements ( $\Delta K_d$ ) for which data for a limited set of 27 mutations was available (**Figure 2d**);  
137 the larger computed RMSE of  $0.81^{1.04}_{0.59}$  kcal/mol represents an estimate of the lower bound of the RMSE to  
138 the  $\text{IC}_{50}$ -derived  $\Delta\Delta G$ s that we might hope to achieve with FEP+ or Prime, which were performed using

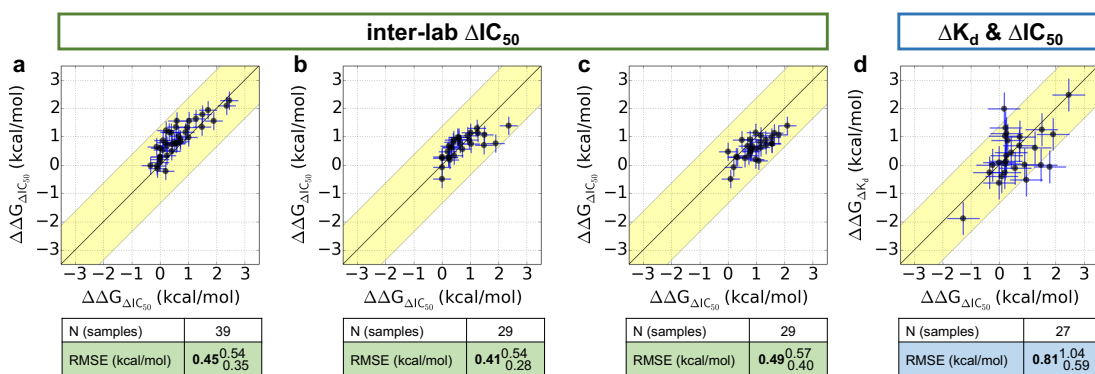


**Figure 2. Cross-comparison of the experimentally measured effects that mutations in Abl kinase have on ligand binding, performed by different labs.**  $\Delta G$  was computed from publicly available  $\Delta pIC_{50}$  or  $\Delta pK_d$  measurements and these values of  $\Delta G$  were then plotted and the RMSE between them reported. (a)  $\Delta pIC_{50}$  measurements (X-axis) from [45] compared with  $\Delta pIC_{50}$  measurements (Y-axis) from [47]. (b)  $\Delta pIC_{50}$  measurements (X-axis) from [45] compared with  $\Delta pIC_{50}$  measurements (Y-axis) from [48]. (c)  $\Delta pIC_{50}$  measurements (X-axis) from [47] compared with  $\Delta pIC_{50}$  measurements (Y-axis) from [48]. (d)  $\Delta pIC_{50}$  measurements (X-axis) from [45] compared with  $\Delta pK_d$  measurements (Y-axis) from [46] using non-phosphorylated Abl kinase. Scatter plot error bars in a,b,c are  $\pm$ standard error (SE) taken from the combined 97 inter-lab  $\Delta \Delta G$ s derived from the  $\Delta pIC_{50}$  measurements, which was  $0.32^{0.36}_{0.28}$ , the RMSE was  $0.45^{0.51}_{0.39}$  kcal/mol. Scatter plot error bars in d are the  $\pm$ standard error (SE) of  $\Delta \Delta G$ s derived from  $\Delta pIC_{50}$  and  $\Delta pK_d$  from a set of 27 mutations, which is  $0.58^{0.74}_{0.42}$ , the RMSE was  $0.81^{1.04}_{0.59}$  kcal/mol.

139 non-phosphorylated models, when comparing sample statistics directly. In comparing 31 mutations for  
 140 which phosphorylated and non-phosphorylated  $\Delta K_d$ s were available, we found a strong correlation between  
 141 the  $\Delta \Delta G$ s derived from those data ( $r=0.94$ , Supplementary *Figure S1*); the statistics of that comparison are  
 142 similar to those of the inter-lab variability comparison.

143 Most clinical mutations do not significantly reduce TKI potency  
 144 The majority of mutations do not lead to resistance by our 10-fold affinity loss threshold: 86.3% of the  
 145 co-crystal set ( $n=113$ ) and 86.8% of the total set ( $n=125$ ). Resistance mutations, which are likely to result in a  
 146 failure of therapy, constitute 13.7% of the co-crystal set ( $n=18$ ) and 13.2% of the total set of mutations ( $n=19$ ).  
 147 The  $\Delta pIC_{50}$ s for all 144 mutations are summarized in *Table S2—Table S7* in the Supplementary Information.  
 148 Two mutations exceeded the dynamic range of the assays ( $IC_{50} > 10,000$  nM); as these two mutations clearly  
 149 raise resistance, we excluded them from quantitative analysis (RMSE and MUE) but included them in truth  
 150 table analyses and classification metrics (accuracy, specificity, sensitivity).

151 How accurately does physical modeling predict affinity changes for clinical Abl mutants?  
 152 From prior experience with relative alchemical free-energy calculations for ligand design, good initial receptor-  
 153 ligand geometry was critical to obtaining accurate and reliable free energy predictions [29], so we first focused  
 154 on the 131 mutations in Abl kinase across six TKIs for which wild-type Abl:TKI co-crystal structures were  
 155 available. *Figure 3* summarizes the performance of predicted binding free-energy changes ( $\Delta \Delta G$ ) for all  
 156 131 mutants in this set for both a fast MM-GBSA physics-based method that only captures interaction  
 157 energies for a single structure (Prime) and rigorous alchemical free-energy calculations (FEP+). Scatter plots  
 158 compare experimental and predicted free-energy changes ( $\Delta \Delta G$ ) and characterize the ability of these two  
 159 techniques to predict experimental measurements. Statistical uncertainty in the predictions and experiment-  
 160 to-experiment variability in the experimental values are shown as ellipse height and widths respectively.  
 161 The value for experimental variability was 0.32 kcal/mol, which was the standard error computed from the  
 162 cross-comparison in *Figure 2*. For FEP+, the uncertainty was taken to be the standard error of the average  
 163 from three independent runs for a particular mutation, while Prime results are deterministic and are not  
 164 contaminated by statistical uncertainty (see Methods).

165 To better assess whether discrepancies between experimental and computed  $\Delta \Delta G$ s simply arise for  
 166 known forcefield limitations or might indicate more significant effects, we incorporated an additional error

167 model in which the forcefield error was taken to be a random error  $\sigma_{FF} \approx 0.9$  kcal/mol, a value established  
168 from previous benchmarks on small molecules absent conformational sampling or protonation state  
169 issues [25]. Thin error bars in **Figure 2** represent the overall estimated error due to both this forcefield error  
170 and experimental variability or statistical uncertainty.

171 To assess overall quantitative accuracy, we computed both root-mean-squared error (RMSE)—which is  
172 rather sensitive to outliers, and mean unsigned error (MUE). For Prime, the MUE was  $1.16^{1.37}_{0.96}$  kcal/mol and  
173 the RMSE was  $1.72^{2.00}_{1.41}$  kcal/mol. FEP+, the alchemical free-energy approach, achieved a significantly higher  
174 level of quantitative accuracy with an MUE of  $0.82^{0.95}_{0.69}$  kcal/mol and an RMSE of  $1.11^{1.30}_{0.91}$  kcal/mol. Notably,  
175 alchemical free energy calculations come substantially closer than MMGBSA approach to the minimum  
176 achievable RMSE of  $0.81^{1.04}_{0.59}$  kcal/mol (due to experimental error; **Figure 2**) for this dataset.

177 How accurately can physical modeling classify mutations as susceptible or resistant?

178 While quantitative accuracy (MUE, RMSE) is a principle metric of model performance, an application of  
179 potential interest is the ability to classify mutations as causing resistance to a specific TKI. To characterize the  
180 accuracy with which Prime and FEP+ classified mutations in a manner that might be therapeutically relevant,  
181 we classified mutations by their experimental impact on the binding affinity as *susceptible* (affinity for mutant  
182 is diminished by no more than 10-fold,  $\Delta\Delta G \leq 1.36$  kcal/mol) or as *resistant* (affinity for mutant is diminished  
183 by least 10-fold,  $\Delta\Delta G > 1.36$  kcal/mol). Summary statistics of experimental and computational predictions of  
184 these classes are shown in **Figure 2** (bottom) as truth tables (also known as *confusion matrices*).

185 The simple minimum-energy scoring method Prime correctly classified 9 of the 18 resistance mutations  
186 in the dataset while merely 85 of the 113 susceptible mutations were correctly classified (28 false positives).  
187 In comparison, the alchemical free-energy method FEP+, which includes entropic and enthalpic contributions  
188 as well as explicit representation of solvent, correctly classified 9 of the 18 resistance mutations while a  
189 vast majority, 105, of the susceptible mutations were correctly classified (merely 8 false positives). Prime  
190 achieved a classification accuracy of  $0.72^{0.79}_{0.64}$ , while FEP+ achieved an accuracy that is significantly higher (both  
191 in a statistical sense and in overall magnitude), achieving an accuracy of  $0.87^{0.92}_{0.81}$ . Sensitivity (also called *true*  
192 *positive rate*) and specificity (*true negative rate*) are also informative statistics in assessing the performance of  
193 a binary classification scheme. For Prime, the sensitivity was  $0.50^{0.73}_{0.25}$ , while the specificity was  $0.75^{0.83}_{0.67}$ . To  
194 put this in perspective, a CML patient bearing a resistance mutation in the kinase domain of Abl has an  
195 equal chance of Prime correctly predicting this mutation would be resistant to one of the TKIs considered  
196 here, while if the mutation was susceptible, the chance of correct prediction would be  $\sim 75\%$ . By contrast,  
197 the classification specificity of FEP+ was substantially better. For FEP+, the sensitivity was  $0.50^{0.74}_{0.29}$  while the  
198 specificity was  $0.93^{0.97}_{0.88}$ . There is a very high probability that FEP+ will correctly predict that one of the eight  
199 TKIs studied here will remain effective for a patient bearing a susceptible mutation.

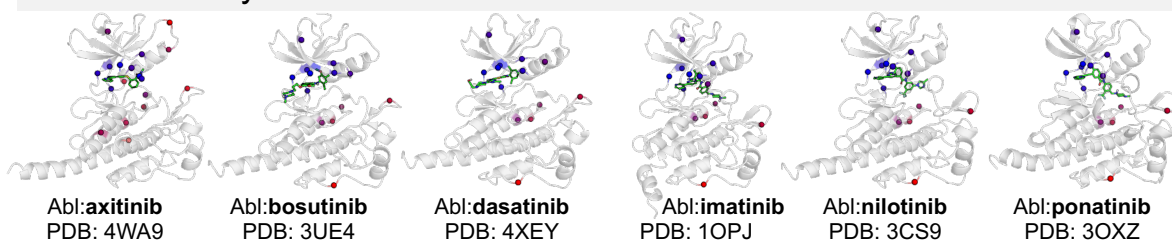
200 How sensitive are classification results to choice of cutoff?

201 Previous work by O'Hare et al. utilized TKI-specific thresholds for dasatinib, imatinib, and nilotinib [49], which  
202 were  $\sim 2$  kcal/mol. Supplementary **Figure S2** shows that when our classification threshold was increased  
203 to a 20-fold change in binding (1.77 kcal/mol), FEP+ correctly classified 8 of the 13 resistant mutations  
204 and with a threshold of 100-fold change in binding (2.72 kcal/mol), FEP+ correctly classified the only two  
205 resistant mutations (T315I/dasatinib and T315I/nilotinib). With the extant multilayered and multinodal  
206 decision-making algorithms used by experienced oncologists to manage their patients' treatment, or by  
207 medicinal chemists to propose candidate compounds for clinical trials, the resistant or susceptible cutoffs  
208 could be selected with more nuance than the simple 10-fold affinity threshold we consider here. With a larger  
209 affinity change cutoff, for example, the accuracy with which physical models predict resistance mutations  
210 increases beyond 90% (Supplementary **Figure S2**). For the alchemical approach, the two-class accuracy was  
211  $0.92^{0.96}_{0.87}$  when an affinity change cutoff of 20-fold was used while using an affinity change cutoff of 100-fold  
212 further improved the two-class accuracy to  $0.98^{1.00}_{0.96}$ .

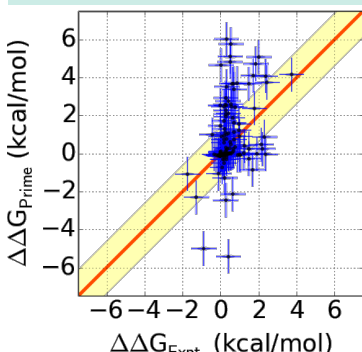
213 Bayesian analysis can estimate the true error

214 The statistical metrics—MUE, RMSE, accuracy, specificity, and sensitivity—discussed above are based on  
215 analysis of the apparent performance of the observed modeling results compared with the observed

## Abl:TKI Co-Crystal Structures

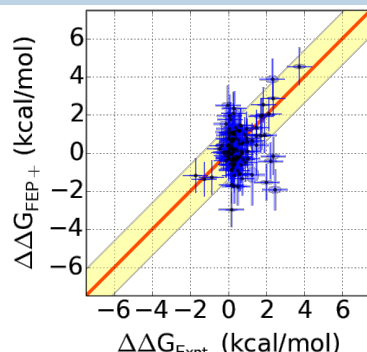


Prime



FEP+

Bootstrap		
<b>MUE</b> (kcal/mol)	<b>1.16</b> 1.37 0.96	<b>0.82</b> 0.95 0.69
<b>RMSE</b> (kcal/mol)	<b>1.72</b> 2.00 1.41	<b>1.11</b> 1.30 0.91
Bayesian Analysis		
<b>MUE</b> (kcal/mol)	<b>*1.40</b> 1.60 1.24	<b>0.79</b> 0.92 0.68
<b>RMSE</b> (kcal/mol)	<b>1.76</b> 2.01 1.55	<b>0.99</b> 1.15 0.85



Prime

Prediction			
		S	r
Experiment	S	85	28
	R	9	9

Bootstrap		
<b>Accuracy</b>	<b>0.72</b> 0.79 0.64	<b>0.87</b> 0.92 0.81
<b>Specificity</b>	<b>0.75</b> 0.83 0.67	<b>0.93</b> 0.97 0.88
<b>Sensitivity</b>	<b>0.50</b> 0.73 0.25	<b>0.50</b> 0.74 0.29
Bayesian Analysis		
<b>Accuracy</b>	<b>0.73</b> 0.76 0.70	<b>0.89</b> 0.92 0.86
<b>Specificity</b>	<b>0.74</b> 0.77 0.72	<b>0.91</b> 0.94 0.89
<b>Sensitivity</b>	<b>0.57</b> 0.77 0.36	<b>0.69</b> 1.00 0.46

FEP+

Prediction			
		S	r
Experiment	S	105	8
	R	9	9

**Figure 3. Comparison of experimentally-measured binding free-energy changes ( $\Delta\Delta G$ ) for 131 clinically observed mutations and 6 selective kinase inhibitors for which co-crystal structures of wild-type kinase with inhibitor are available. Top panel:** Abl:TKI co-crystal structures used in this study with locations of clinical mutants for each inhibitor highlighted (colored from blue to red for residues nearest to farthest from ligand) in relation to TKI (green sticks) on the corresponding Abl:TKI wild-type crystal structure. **Middle panel:** Scatter plots show Prime and FEP+ computed  $\Delta\Delta G$  compared to experiment, with ellipse widths and heights ( $\pm\sigma$ ) for experiment and FEP+ respectively. The red diagonal line indicates when prediction equals experiment, while the yellow shaded region indicates area in which predicted  $\Delta\Delta G$  is within 1.36 kcal/mol of experiment (corresponding to a ten-fold error in predicted affinity change).  $\Delta\Delta G < 0$  denotes the mutation increases the susceptibility of the kinase to the inhibitor, while  $\Delta\Delta G > 0$  denotes the mutation increases the resistance of the kinase to the inhibitor. The two mutations that were beyond the concentration limit of the assay (T315I/dasatinib, L248R/imatinib) were not plotted; 129 points were plotted. Truth tables of classification accuracy, sensitivity and specificity using two-classes. **Bottom panel:** Truth tables and classification results include T315I/dasatinib and L248R/imatinib; 131 points were used. For MUE, RMSE, and truth table performance statistics, sub/superscripts denote 95 % CIs. Variability in the experimental data is shown as ellipse widths and uncertainty in our calculations is shown as ellipse heights. Experimental variability was computed as the standard error between  $IC_{50}$ -derived  $\Delta\Delta G$  measurements made by different labs, 0.32 kcal/mol. The statistical uncertainty in the Prime calculations was zero because the method is deterministic ( $\sigma_{cal} = 0$ ), while the uncertainty in the FEP+ calculations was reported as the standard error,  $\sigma_{cal}$ , of the mean of the predicted  $\Delta\Delta G$ s from three independent runs. To better highlight true outliers unlikely to simply result from expected forcefield error, we presume forcefield error ( $\sigma_{FF} \approx 0.9$  kcal/mol [25]) also behaves as a random error, and represent the total estimated statistical and forcefield error ( $\sqrt{\sigma_{FF}^2 + \sigma_{exp/cal}^2}$ ) as vertical error bars. The horizontal error bars for the experiment ( $\sigma_{exp}$ ) was computed as the standard error between  $\Delta pIC_{50}$  and  $\Delta K_d$  measurements, 0.58 kcal/mol. For Prime, \*MUE highlights that the Bayesian model yields a value for MUE that is noticeably larger than MUE for observed data due to the non-Gaussian error distribution of Prime.

216 experimental data via sample statistics. However, this analysis considers a limited number of mutants,  
217 and both measurements and computed values are contaminated with experimental or statistical error.  
218 To obtain an estimate of the *intrinsic performance* of our physical modeling approaches, accounting for  
219 known properties of the experimental variability and statistical uncertainties, we used a hierarchical Bayesian  
220 model (detailed in the Methods) to infer posterior predictive distributions from which expectations and 95%  
221 predictive intervals could be obtained. The results of this analysis are presented in **Figure 3** (central tables).

222 FEP+ is significantly better than Prime at predicting the impact of mutations on TKI binding affinities, as the  
223 apparent performance (using the original observations) as well as the intrinsic performance (where Bayesian  
224 analysis was used to correct for statistical uncertainty or experimental variation) were well-separated outside  
225 their 95% confidence intervals in nearly all metrics. Applying the Bayesian model, the MUE and RMSE for  
226 FEP+ was  $0.79^{0.92}_{0.68}$  kcal/mol and  $0.99^{1.15}_{0.85}$  kcal/mol respectively (N=129). For the classification metrics accuracy,  
227 specificity, and sensitivity, the model yields  $0.89^{0.92}_{0.86}$ ,  $0.91^{0.94}_{0.89}$ , and  $0.69^{1.00}_{0.46}$  respectively (N=131). The intrinsic  
228 RMSE and MUE of Prime was  $1.76^{2.01}_{1.55}$  kcal/mol and  $1.40^{1.60}_{1.24}$  kcal/mol (N=129) respectively, and the classification  
229 accuracy, specificity, and sensitivity was  $0.73^{0.76}_{0.70}$ ,  $0.74^{0.77}_{0.72}$ , and  $0.57^{0.77}_{0.36}$  respectively (N=131). The intrinsic MUE of  
230 Prime obtained by this analysis is larger than the observed MUE reflecting the non-Gaussian, fat-tailed error  
231 distributions of Prime results.

232 Is the impact of point mutations on drug binding equally well-predicted for the six TKIs?  
233 The impact of point mutations on drug binding are not equally well predicted for the six TKIs. **Figure 4**  
234 expands the results in **Figure 3** on a TKI-by-TKI basis to dissect the particular mutations in the presence of  
235 a specific TKI. Prime and FEP+ correctly predicted that most mutations in this dataset (N=26) do not raise  
236 resistance to axitinib, though FEP+ predicted 4 false positives compared with 3 false positives by Prime. The  
237 MUE and RMSE of FEP+ was excellent for this inhibitor,  $0.70^{0.93}_{0.50}$  kcal/mol and  $0.91^{1.14}_{0.64}$  kcal/mol respectively.  
238 While the classification results for bosutinib (N=21) were equally well predicted by Prime as by FEP+, FEP+ was  
239 still able to achieve superior, but not highly significant, predictive performance for the quantitative metrics  
240 MUE and RMSE, which were  $0.96^{1.42}_{0.55}$  kcal/mol and  $1.41^{1.97}_{0.77}$  kcal/mol respectively (FEP+) and  $1.13^{1.83}_{0.60}$  kcal/mol and  
241  $1.80^{2.62}_{0.92}$  kcal/mol respectively (Prime). For dasatinib, FEP+ achieved an MUE and RMSE of  $0.76^{1.13}_{0.49}$  kcal/mol and  
242  $1.07^{1.57}_{0.59}$  kcal/mol respectively whereas the results were, as expected, less quantitatively predictive for Prime  
243 (N=20). The results for imatinib were similar to those of dasatinib above, where the MUE and RMSE for FEP+  
244 were  $0.82^{1.15}_{0.53}$  kcal/mol and  $1.09^{1.43}_{0.69}$  kcal/mol respectively (N=20). Nilotinib, a derivative of imatinib, led to nearly  
245 identical quantitative performance results for FEP+ with an MUE and RMSE of  $0.82^{1.12}_{0.57}$  kcal/mol and  $1.06^{1.39}_{0.69}$   
246 kcal/mol respectively (N=21). Similar to axitinib, ponatinib presented an interesting case because there were  
247 no mutations in this dataset that raised resistance to it. Despite the wide dynamic range in the computed  
248 values of  $\Delta\Delta G$  for other inhibitors, FEP+ correctly predicted a very narrow range of  $\Delta\Delta G$ s for this drug. This  
249 is reflected in the MUE and RMSE of  $0.87^{1.16}_{0.62}$  kcal/mol and  $1.09^{1.46}_{0.70}$  kcal/mol respectively, which are in-line with  
250 the MUEs and RMSEs for the other TKIs.

251 Understanding the origin of mispredictions

252 Resistance mutations that are mispredicted as susceptible (false negatives) are particularly critical because  
253 they might mislead the clinician or drug designer into believing the inhibitor will remain effective against  
254 the target. Which resistance mutations did FEP+ mispredict as susceptible? Nine mutations were classified  
255 by FEP+ to be susceptible when experimentally measured  $\Delta pIC_{50}$  data indicate the mutations should have  
256 increased resistance according to our 10-fold affinity cutoff for resistance. Notably, the 95% confidence  
257 intervals for five of these mutations spanned the 1.36 kcal/mol threshold, indicating these misclassifications  
258 are not statistically significant when the experimental error and statistical uncertainty in FEP+ are accounted for:  
259 bosutinib/L248R ( $\Delta\Delta G_{FEP+} = 1.32^{1.94}_{0.70}$  kcal/mol), imatinib/E255K ( $\Delta\Delta G_{FEP+} = 0.43^{3.05}_{-2.19}$  kcal/mol), imatinib/Y253F  
260 ( $\Delta\Delta G_{FEP+} = 0.95^{1.64}_{0.26}$  kcal/mol), and nilotinib/Y253F ( $\Delta\Delta G_{FEP+} = 0.89^{1.69}_{0.09}$  kcal/mol). The bosutinib/V299L mutation  
261 was also not significant because the experimental  $\Delta\Delta G$ ,  $1.70^{2.33}_{1.08}$  kcal/mol, included the 1.36 kcal/mol cutoff;  
262 the value of  $\Delta\Delta G$  predicted by FEP+ for this mutation was  $0.91^{1.02}_{0.79}$  kcal/mol, the upper bound of the predicted  
263 value was within 0.06 kcal/mol of the lower bound of the experimental value.

264 Four mutations, however, were misclassified to a degree that is statistically significant given their 95% con-

265 fidence intervals: dasatinib/T315A, bosutinib/T315I, imatinib/E255V, and nilotinib/E255V. For dasatinib/T315A,  
266 although the T315A mutations for bosutinib, imatinib, nilotinib, and ponatinib were correctly classified as  
267 susceptible, the predicted free energy changes for these four TKIs were consistently much more negative  
268 than the corresponding experimental measurements, just as for dasatinib/T315A, indicating there might be a  
269 generic driving force contributing to the errors in T315A mutations for these five TKIs. Abl is known to be able  
270 to adopt many different conformations (including DFG-in and DFG-out), and it is very likely that the T315A  
271 mutation will induce conformational changes in the apo protein [50], which was not adequately sampled in  
272 the relatively short simulations, leading to the errors for T315A mutations for these TKIs. By comparison,  
273 the T315I mutations for axitinib, bosutinib, imatinib, nilotinib, and ponatinib were all accurately predicted  
274 with the exception of bosutinib/T315I being the only misprediction, suggesting an issue specific to bosutinib.  
275 The complex electrostatic interactions between the 2,4-dichloro-5-methoxyphenyl ring in bosutinib and the  
276 adjacent positively charged amine of the catalytic Lys271 may not be accurately captured by the fixed-charge  
277 OPLS3 force field, leading to the misprediction for bosutinib/T315I mutation.

278 Insufficient sampling might also belie the imatinib/E255V and nilotinib/E255V mispredictions because  
279 they reside in the highly flexible P-loop. Since E255V was a charge change mutation, we utilized a workflow  
280 that included a transmutable explicit ion (see Methods). The distribution of these ions in the simulation box  
281 around the solute might not have converged to their equilibrium state on the relatively short timescale of  
282 our simulations (5 ns), and the insufficient sampling of ion distributions coupled with P-loop motions might  
283 lead to misprediction of these two mutations.

284 How accurately can the impact of mutations be predicted for docked TKIs?

285 To assess the potential for utilizing physics-based approaches in the absence of a high-resolution experimen-  
286 tal structure, we generated models of Abl bound to two TKIs—erlotinib and gefitinib—for which co-crystal  
287 structures with wild-type kinase are not currently available. In **Figure 5**, we show the Abl:erlotinib and  
288 Abl:gefitinib complexes that were generated using a docking approach (Glide-SP, see Methods). These two  
289 structures were aligned against the co-crystal structures of EGFR:erlotinib and EGFR:gefitinib to highlight the  
290 structural similarities between the binding pockets of Abl and EGFR and the TKI binding mode in Abl versus  
291 EGFR. As an additional test of the sensitivity of FEP+ to system preparation, a second set of Abl:erlotinib and  
292 Abl:gefitinib complexes was generated in which crystallographic water coordinates were transferred to the  
293 docked inhibitor structures (see Methods).

294 Alchemical free-energy simulations were performed on 13 mutations between the two complexes; 7  
295 mutations for erlotinib and 6 mutations for gefitinib. The quantitative accuracy of FEP+ in predicting the  
296 value of  $\Delta\Delta G$  was excellent—MUE and RMSE of  $0.58_{-0.33}^{0.86}$  kcal/mol and  $0.80_{-0.44}^{0.09}$  kcal/mol respectively if crystal  
297 waters are omitted, and  $0.50_{-0.26}^{0.78}$  kcal/mol and  $0.69_{-0.35}^{0.97}$  kcal/mol if crystal waters were restored after docking.  
298 Encouragingly, these results indicate that our initial models of Abl bound to erlotinib and gefitinib were  
299 reliable because the accuracy and dependability of our FEP+ calculations were not sensitive to crystallographic  
300 waters. Our secondary concern was the accuracy with which the approach classified mutations as resistant  
301 or susceptible.

302 While the results presented in (**Figure 5**) indicate that FEP+ is capable of achieving good quantitative  
303 accuracy when a co-crystal structure is unavailable, it is important to understand why a mutation was  
304 predicted to be susceptible but was determined experimentally to be resistant. F317I was the one mutation  
305 that increased resistance to erlotinib (or gefitinib) because it destabilized binding by more than 1.36 kcal/mol—  
306  $1.35_{-1.03}^{1.67}$  kcal/mol (gefitinib) and  $1.58_{-1.26}^{1.90}$  kcal/mol (erlotinib), but the magnitude of the experimental uncertainty  
307 means we are unable to confidently discern whether this mutation induces more than 10-fold resistance  
308 to either TKI. Therefore, the one misclassification by FEP+ in **Figure 5** is not statistically significant and the  
309 classification metrics presented there underestimate the nominal performance of this alchemical free-energy  
310 method.

## 311 Discussion

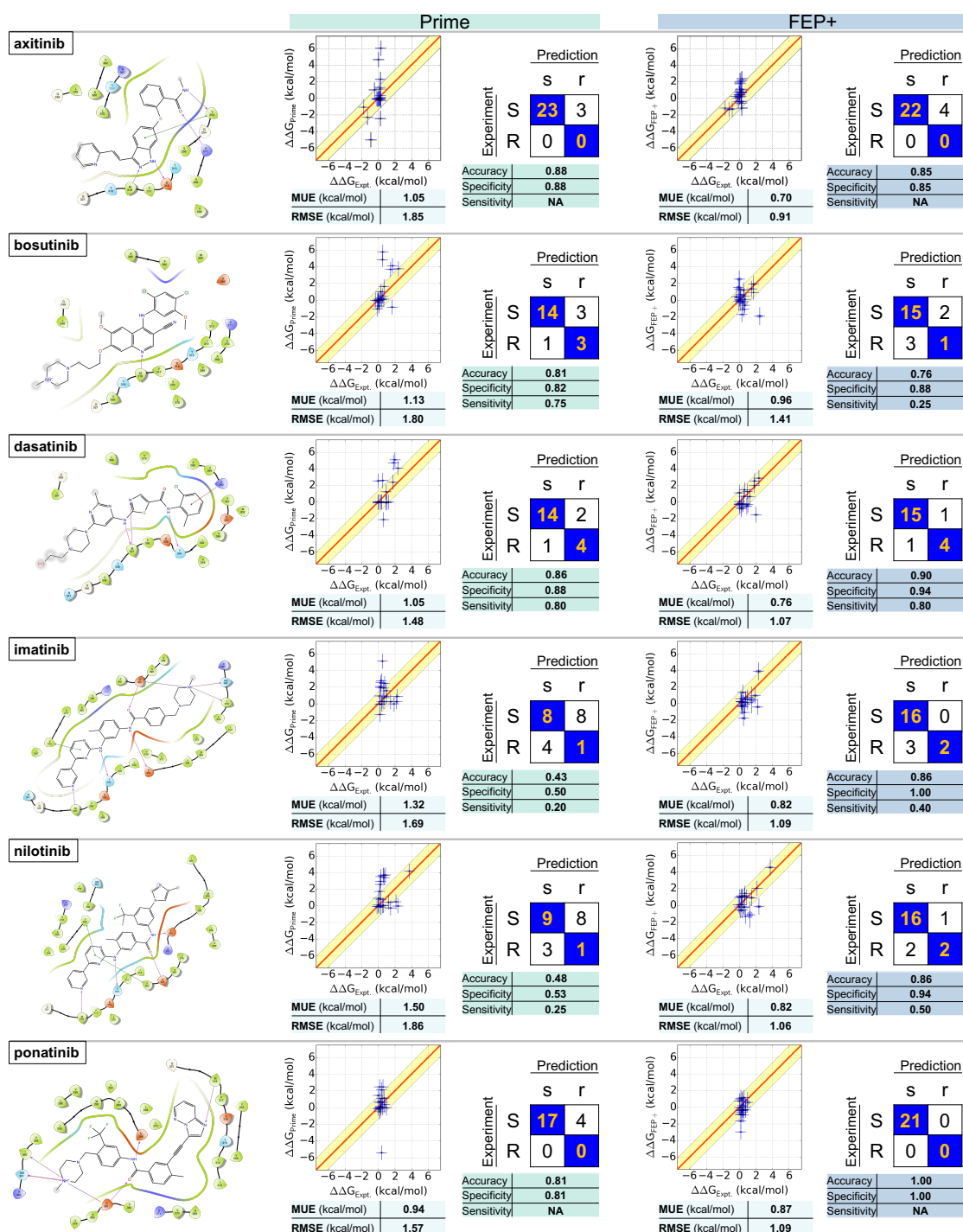


**Figure 4. Physical modeling accuracy in computing the impact of clinical Abl mutations on selective inhibitor binding.** Ligand interaction diagrams for six selective FDA-approved tyrosine kinase inhibitors (TKIs) for which co-crystal structures with Abl were available (left). Comparisons for clinically-observed mutations are shown for FEP+ (right) and Prime (left). For each ligand, computed vs. experimental binding free energies ( $\Delta\Delta G$ ) are plotted with MUE and RMSE (units of kcal/mol) depicted below. Truth tables are shown to the right. Rows denote *true* susceptible (S,  $\Delta\Delta G \leq 1.36$  kcal/mol) or resistant (R,  $\Delta\Delta G > 1.36$  kcal/mol) experimental classes using a 1.36 kcal/mol (10-fold change) threshold; columns denote *predicted* susceptible (s,  $\Delta\Delta G \leq 1.36$  kcal/mol) or resistant (r,  $\Delta\Delta G > 1.36$  kcal/mol). Correct predictions populate diagonal elements (orange text), incorrect predictions populate off-diagonals. Accuracy, specificity, and sensitivity for two-class classification are shown below the truth table. Elliptical point sizes and error bars in the scatter plots depict estimated uncertainty/variability and error respectively ( $\pm\sigma$ ) of FEP+ values (vertical size) and experimental values (horizontal size). Note: The sensitivity for axitinib and ponatinib is NA, because there is no resistant mutation for these two drugs.

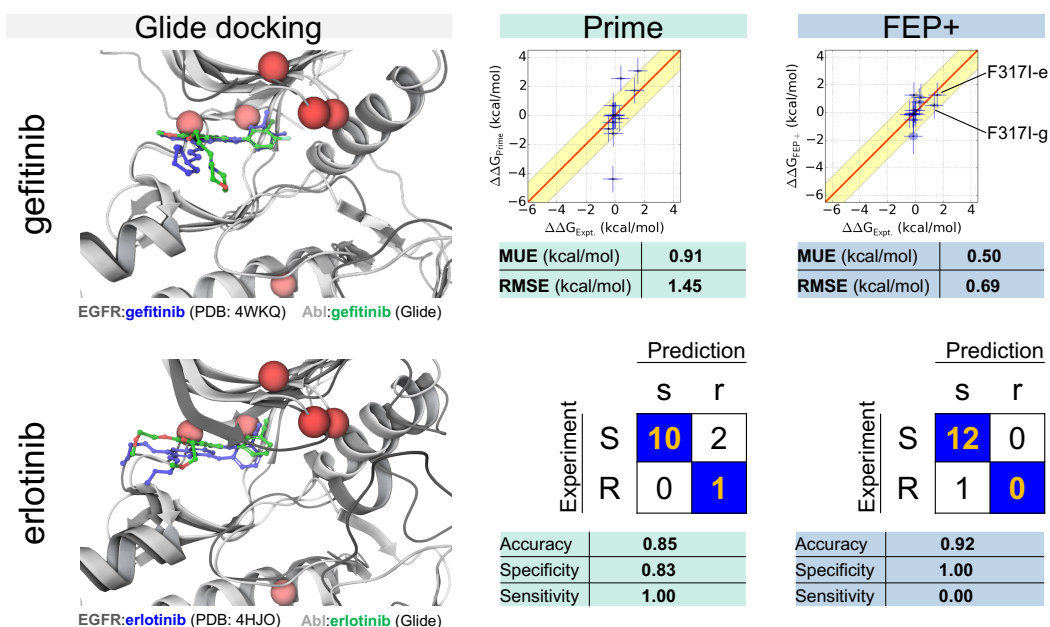


**Figure 5. Predicting resistance mutations using FEP+ for inhibitors for which co-crystal structures with wild-type kinase are not available.** The docked pose of Abl:erlotinib is superimposed on the co-crystal structure of EGFR:erlotinib; erlotinib docked to Abl (light gray) is depicted in green and erlotinib bound to EGFR (dark gray) is depicted in blue. The docked pose of Abl:gefitinib is superimposed on the co-crystal structure of EGFR:gefitinib; gefitinib docked to Abl (light gray) is depicted in green and gefitinib bound to EGFR (dark gray) is depicted in blue. The locations of clinical mutants for each inhibitor are highlighted (red spheres). The overall RMSEs and MUEs for Prime (center) and FEP+ (right) and two-class accuracies are also shown in the figure. Computed free energy changes due to the F317I mutation for erlotinib (-e) and gefitinib (-g) are highlighted in the scatter plot. FEP+ results are based on the docked models prepared with crystal waters added back while the Prime (an implicit solvent model) results are based on models without crystallographic water.

312 Physics-based modeling can reliably predict when a mutation elicits resistance to therapy  
313 The results presented in this work are summarized in **Table 2**. The performance metrics summarized in  
314 **Table 2** indicates that the set of 131 mutations for the six TKIs in which co-crystal structures were available is  
315 on par with the complete set (144 mutations), which included results based on Abl:TKI complexes generated  
316 from docking models. The performance results for the 13 mutations for the two TKIs (erlotinib and gefitinib)  
317 in which co-crystal structures were unavailable exhibited good quantitative accuracy (MUE and RMSE) and  
318 good classification power.

319 Overall (N=144), the MM-GBSA approach Prime classified mutations with good accuracy ( $0.73^{0.80}_{0.66}$ ) and  
320 specificity ( $0.76^{0.84}_{0.69}$ ) while the alchemical approach FEP+ was a significant improvement in classification  
321 accuracy ( $0.88^{0.93}_{0.82}$ ) and specificity ( $0.94^{0.98}_{0.89}$ ). The quantitative accuracy with which Prime was able to predict the  
322 experimentally measured change in Abl:TKI binding (N=142) characterized by RMSE and MUE was  $1.70^{1.98}_{1.40}$   
323 kcal/mol and  $1.14^{1.35}_{0.93}$  kcal/mol respectively. In stark contrast, the quantitative accuracy of FEP+ was statistically  
324 superior to Prime with an RMSE and an MUE of  $1.07^{1.26}_{0.89}$  kcal/mol and  $0.79^{0.92}_{0.67}$  kcal/mol respectively.

325 From the perspective of a clinician, classification rate would be an important metric to measure the  
326 predictive power of technologies such as Prime and FEP+. To test the hypothesis that reducing the large  
327 spread in Prime predictions could improve its classification rate, we scaled the computed relative free  
328 energies (by 1/2, 1/3, and by 0.23, which was the optimal factor that gives lowest RMSE) and recalculated  
329 the classification metrics (**Table S8**). As expected, the MUE and RMSE were improved but the specificity of  
330 Prime was drastically diminished; as MUE and RMSE improved, it became increasingly unable to identify  
331 resistance mutations. Scaling FEP+ eliminated its sensitivity and a naïve model (where all free energies were  
332 set to 0.00 kcal/mol) had zero sensitivity. Lastly, we constructed a consensus model in which free energies  
333 were a weighted average of scaled Prime and FEP+. However, this model also had no sensitivity. It appears  
334 difficult to improve upon the predictive power of FEP+ by statistical operations.

335 To address the impact of picking a cutoff to classify predicted free energies as resistant or sensitizing, we  
336 computed ROC curves for the various predicted datasets: Prime (scaled and non-scaled), FEP+ (scaled and  
337 non-scaled), naïve model, and consensus model (constructed from scaled Prime and scaled FEP+, see above).  
338 ROC curves are independent of a linear transformation on the predicted dataset. Therefore, ROC curves  
339 and ROC-AUCs for scaled and non-scaled Prime were identical, as well as scaled and non-scaled FEP+. ROC  
340 curves for these six sets of predictions are presented in Supplementary **Figure S3**. ROC-AUC for FEP+ was  
341  $0.75^{0.90}_{0.61}$  (n=144); ROC-AUC for Prime was  $0.66^{0.81}_{0.52}$  (n=144); ROC-AUCs for the naïve model and consensus model  
342 were  $0.50^{0.50}_{0.50}$  (n=144) and  $0.78^{0.90}_{0.67}$  (n=144) respectively. These results show that Prime apparently has poor  
343 discriminatory power (ROC-AUC in [0.6,0.7]) while FEP+ apparently has fair discriminatory power (ROC-AUC  
344 in [0.7,0.8]).

345 Hierarchical Bayesian model estimates global performance (N=144)

346 A hierarchical Bayesian approach was developed to estimate the intrinsic accuracy of the models when the  
347 noise in the experimental and predicted values of  $\Delta\Delta G$  was accounted for. Utilizing this approach, the MUE  
348 and RMSE for Prime was found to be  $1.39^{1.58}_{1.23}$  kcal/mol and  $1.75^{1.98}_{1.55}$  kcal/mol (N=142) respectively. The accuracy,  
349 specificity, and sensitivity of Prime was found using this method to be  $0.74^{0.76}_{0.71}$ ,  $0.75^{0.77}_{0.73}$ , and  $0.59^{0.78}_{0.40}$  (N=144)  
350 respectively. The MUE and RMSE of FEP+ was found to be  $0.76^{0.87}_{0.66}$  kcal/mol and  $0.95^{1.09}_{0.82}$  kcal/mol (N=142)  
351 respectively, which is significantly better than Prime. Likewise, a clearer picture of the true classification  
352 accuracy, specificity, and sensitivity of FEP+ was found— $0.90^{0.93}_{0.86}$ ,  $0.92^{0.95}_{0.90}$ , and  $0.68^{1.00}_{0.46}$  respectively.

### 353 **Examining the physical and chemical features of outliers**

354 Current alchemical approaches neglect effects that will continue to improve accuracy

355 The high accuracy of FEP+ is very encouraging, and the accuracy can be further improved with more accurate  
356 modeling of a number of physical chemical effects not currently considered by the method. While highly  
357 optimized, the fixed-charged OPLS3 [25] force field can be further improved by explicit consideration of  
358 polarizability effects [51], as hinted by some small-scale benchmarks [52]. These features could be especially  
359 important for bosutinib, whose 2,4-dichloro-5-methoxyphenyl ring is adjacent to the positively charged amine  
360 of the catalytic Lys271. Many simulation programs also utilize a long-range isotropic analytical dispersion

**Table 2. Summary of FEP+ and Prime statistics in predicting mutational resistance or sensitivity to FDA-approved TKIs.**

Dataset	Method	N <sub>quant</sub>	MUE (kcal/mol)	RMSE (kcal/mol)	N <sub>class</sub>	Accuracy	Specificity	Sensitivity
all	FEP+	142	0.79 <sup>0.92</sup> <sub>0.67</sub>	1.07 <sup>1.26</sup> <sub>0.89</sub>	144	0.88 <sup>0.93</sup> <sub>0.82</sub>	0.94 <sup>0.98</sup> <sub>0.89</sub>	0.47 <sup>0.69</sup> <sub>0.25</sub>
all	Prime	142	1.14 <sup>1.35</sup> <sub>0.93</sub>	1.70 <sup>1.98</sup> <sub>1.40</sub>	144	0.73 <sup>0.80</sup> <sub>0.66</sub>	0.76 <sup>0.84</sup> <sub>0.69</sub>	0.53 <sup>0.76</sup> <sub>0.30</sub>
xtals	FEP+	129	0.82 <sup>0.95</sup> <sub>0.69</sub>	1.11 <sup>1.30</sup> <sub>0.91</sub>	131	0.87 <sup>0.92</sup> <sub>0.81</sub>	0.93 <sup>0.97</sup> <sub>0.88</sub>	0.50 <sup>0.74</sup> <sub>0.29</sub>
xtals	Prime	129	1.16 <sup>1.37</sup> <sub>0.96</sub>	1.72 <sup>2.00</sup> <sub>1.41</sub>	131	0.72 <sup>0.79</sup> <sub>0.64</sub>	0.75 <sup>0.83</sup> <sub>0.67</sub>	0.50 <sup>0.73</sup> <sub>0.25</sub>
axitinib	FEP+	26	0.70 <sup>0.93</sup> <sub>0.50</sub>	0.91 <sup>1.14</sup> <sub>0.64</sub>	26	0.85 <sup>0.96</sup> <sub>0.69</sub>	0.85 <sup>0.96</sup> <sub>0.69</sub>	NA
axitinib	Prime	26	1.05 <sup>1.71</sup> <sub>0.53</sub>	1.85 <sup>2.61</sup> <sub>0.96</sub>	26	0.88 <sup>1.00</sup> <sub>0.73</sub>	0.88 <sup>1.00</sup> <sub>0.73</sub>	NA
bosutinib	FEP+	21	0.96 <sup>1.42</sup> <sub>0.55</sub>	1.41 <sup>1.97</sup> <sub>0.77</sub>	21	0.76 <sup>0.95</sup> <sub>0.57</sub>	0.88 <sup>1.00</sup> <sub>0.71</sub>	0.25 <sup>1.00</sup> <sub>0.00</sub>
bosutinib	Prime	21	1.13 <sup>1.83</sup> <sub>0.60</sub>	1.80 <sup>2.62</sup> <sub>0.92</sub>	21	0.81 <sup>0.95</sup> <sub>0.62</sub>	0.82 <sup>1.00</sup> <sub>0.62</sub>	0.75 <sup>1.00</sup> <sub>0.00</sub>
dasatinib	FEP+	20	0.76 <sup>1.13</sup> <sub>0.49</sub>	1.07 <sup>1.57</sup> <sub>0.59</sub>	21	0.90 <sup>1.00</sup> <sub>0.76</sub>	0.94 <sup>1.00</sup> <sub>0.79</sub>	0.80 <sup>1.00</sup> <sub>0.33</sub>
dasatinib	Prime	20	1.05 <sup>1.54</sup> <sub>0.61</sub>	1.48 <sup>1.92</sup> <sub>0.95</sub>	21	0.86 <sup>1.00</sup> <sub>0.71</sub>	0.88 <sup>1.00</sup> <sub>0.69</sub>	0.80 <sup>1.00</sup> <sub>0.33</sub>
imatinib	FEP+	20	0.82 <sup>1.15</sup> <sub>0.53</sub>	1.09 <sup>1.43</sup> <sub>0.69</sub>	21	0.86 <sup>1.00</sup> <sub>0.71</sub>	1.00 <sup>1.00</sup> <sub>1.00</sub>	0.40 <sup>0.83</sup> <sub>0.00</sub>
imatinib	Prime	20	1.32 <sup>1.81</sup> <sub>0.91</sub>	1.69 <sup>2.26</sup> <sub>1.15</sub>	21	0.43 <sup>0.67</sup> <sub>0.24</sub>	0.50 <sup>0.75</sup> <sub>0.25</sub>	0.20 <sup>0.67</sup> <sub>0.00</sub>
nilotinib	FEP+	21	0.82 <sup>1.12</sup> <sub>0.57</sub>	1.06 <sup>1.39</sup> <sub>0.69</sub>	21	0.86 <sup>1.00</sup> <sub>0.67</sub>	0.94 <sup>1.00</sup> <sub>0.80</sub>	0.50 <sup>1.00</sup> <sub>0.00</sub>
nilotinib	Prime	21	1.50 <sup>1.97</sup> <sub>1.06</sub>	1.86 <sup>2.25</sup> <sub>1.43</sub>	21	0.48 <sup>0.67</sup> <sub>0.24</sub>	0.53 <sup>0.75</sup> <sub>0.29</sub>	0.25 <sup>1.00</sup> <sub>0.00</sub>
ponatinib	FEP+	21	0.87 <sup>1.16</sup> <sub>0.62</sub>	1.09 <sup>1.46</sup> <sub>0.70</sub>	21	1.00 <sup>1.00</sup> <sub>1.00</sub>	1.00 <sup>1.00</sup> <sub>1.00</sub>	NA
ponatinib	Prime	21	0.94 <sup>1.54</sup> <sub>0.50</sub>	1.57 <sup>2.44</sup> <sub>0.69</sub>	21	0.81 <sup>0.95</sup> <sub>0.62</sub>	0.81 <sup>0.95</sup> <sub>0.62</sub>	NA
Glide	FEP+	13	0.50 <sup>0.78</sup> <sub>0.26</sub>	0.69 <sup>0.97</sup> <sub>0.35</sub>	13	0.92 <sup>1.00</sup> <sub>0.77</sub>	1.00 <sup>1.00</sup> <sub>1.00</sub>	0.00 <sup>0.00</sup> <sub>0.00</sub>
Glide	Prime	13	0.91 <sup>1.56</sup> <sub>0.39</sub>	1.45 <sup>2.22</sup> <sub>0.54</sub>	13	0.85 <sup>1.00</sup> <sub>0.62</sub>	0.83 <sup>1.00</sup> <sub>0.58</sub>	1.00 <sup>1.00</sup> <sub>0.00</sub>

N<sub>quant</sub>: Number of mutations for which quantitative metrics were evaluated; N<sub>class</sub>: Number mutations for which classification metrics were evaluated; All: All mutations; xtals: All mutations for which co-crystal structures were available; Glide: erlotinib and gefitinib

Accuracy, specificity, and sensitivity were computed to assess two-class prediction performance:

resistant ( $\Delta\Delta G > 1.36$  kcal/mol) or susceptible ( $\Delta\Delta G \leq 1.36$  kcal/mol).

95% CIs (sub-/superscripts) were estimated from 1000 bootstrap replicates. Note: The sensitivity for axitinib and ponatinib is NA, because there is no resistant mutation for these two drugs.

361 correction intended to correct for the truncation of dispersion interactions at finite cutoff, which can induce  
 362 an error in protein-ligand binding free energies that depends on the number of ligand heavy atoms being  
 363 modified [53]; recently, efficient Lennard-Jones PME methods [54, 55] and perturbation schemes [53] have  
 364 been developed that can eliminate the errors associated with this truncation. While the currently employed  
 365 methodology for alchemical transformations involving a change in system charge (see Methods) reduces  
 366 artifacts that depend on the simulation box size and periodic boundary conditions, the explicit ions that were  
 367 included in these simulations may not have sufficiently converged to their equilibrium distributions in these  
 368 relatively short simulations. Kinases and their inhibitors are known to possess multiple titratable sites with  
 369 either intrinsic or effective pK<sub>a</sub>s near physiological pH, while the simulations here treat protonation states  
 370 and proton tautomers fixed throughout the bound and unbound states; the accuracy of the model can be  
 371 further improved with the protonation states or tautomers shift upon binding or mutation considered [56, 57].  
 372 Similarly, some systems display significant salt concentration dependence [58], while the simulations for  
 373 some systems reported here did not rigorously mimic all aspects of the experimental conditions of the cell  
 374 viability assays.

375 Experimentally observed IC<sub>50</sub> changes can be caused by other physical mechanisms  
 376 While we have shown that predicting the direct impact of mutations on the binding affinity of ATP-competitive  
 377 tyrosine kinase inhibitors for a single kinase conformation has useful predictive capacity, many additional  
 378 physical effects that can contribute to cell viability are not currently captured by examining only the predicted  
 379 change in inhibitor binding affinity. For example, kinase missense mutations can also shift the populations

380 of kinase conformations (which may affect ATP and inhibitor affinities differentially), modulate ATP affinity,  
381 modulate affinity for protein substrate, or modulate the ability of the kinase to be regulated or bounded  
382 by scaffolding proteins. These physical mechanisms might affect the  $IC_{50}$ s of cell viability assays but not  
383 necessarily the binding affinity of the inhibitors. While many of these effects are in principle tractable by  
384 physical modeling in general (and alchemical free energy methods in particular), it is valuable to examine our  
385 mispredictions and outliers to identify whether any of these cases is likely to induce resistance (as observed  
386 by  $\Delta IC_{50}$  shifts) by one of these alternative mechanisms.

387 Other physical mechanisms of resistance are likely similarly computable.

388 A simple threshold of 10-fold TKI affinity change is a crude metric for classifying resistance or susceptibility  
389 due to the myriad biological factors that contribute to the efficacy of a drug in a person. Except for affecting  
390 the binding affinity of inhibitors, missense mutations can also cause drug resistance through other physical  
391 mechanisms including induction of splice variants or alleviation of feedback. While the current study only  
392 focused on the effect of mutation on drug binding affinity, resistance from these other physical mechanisms  
393 could be similarly computed using physical modeling. For example, some mutations are known to activate  
394 the kinase by increasing affinity to ATP, which could be computed using the same thermodynamic cycle  
395 utilized here for inhibitors.

## 396 Conclusion

397 Revolutionary changes in computing power—especially the arrival of inexpensive graphics processors  
398 (GPUs)—and software automation have enabled alchemical free-energy calculations to impact drug discovery  
399 and life sciences projects in previously unforeseen ways. In this communication, we tested the hypothesis  
400 that FEP+, a fully-automated relative-alchemical free-energy workflow, had reached the point where it can  
401 accurately and reliably predict how clinically-observed mutations in Abl kinase alter the binding affinity of  
402 eight FDA-approved TKIs. To establish the potential predictive impact of current-generation alchemical free  
403 energy calculations—which incorporate entropic and enthalpic effects and the discrete nature of aqueous  
404 solvation—compared to a simpler physics-based approach that also uses modern forcefields but scores a  
405 single minimized conformation, we employed a second physics-based approach (Prime). This simpler physics-  
406 based model, which uses an implicit model of solvation to score the energetic changes in interaction energy  
407 that arise from the mutation, was able to capture a useful amount of information to achieve substantial  
408 predictiveness with an MUE of  $1.14^{1.35}_{0.93}$  kcal/mol (N=142), RMSE of  $1.70^{1.98}_{1.40}$  kcal/mol respectively (N=142), and  
409 classification accuracy of  $0.73^{0.80}_{0.66}$  (N=144). Surpassing these good results, we went on to demonstrate that  
410 FEP+ is able to achieve superior predictive performance—MUE of  $0.79^{0.92}_{0.67}$  kcal/mol (N=142), RMSE of  $1.07^{1.26}_{0.89}$   
411 kcal/mol (N=142), and classification accuracy of  $0.88^{0.93}_{0.82}$  (N=144). While future enhancements to the workflows  
412 for Prime and FEP+ to account for additional physical and chemical effects are likely to improve predictive  
413 performance further, the present results are of sufficient quality and achievable on a sufficiently rapid  
414 timescale (with turnaround times ~6 hours/calculation) to impact research projects in drug discovery and the  
415 life sciences. With exponential improvements in computing power, we anticipate the domains of applicability  
416 for alchemical free-energy methods such as FEP+ will take on increasingly integrated roles to impact projects.  
417 This work illustrates how the domain of applicability for alchemical free-energy methods is much larger  
418 than previously appreciated, and might further be found to include new areas as research progresses:  
419 aiding clinical decision-making in the selection of first- or second-line therapeutics guided by knowledge  
420 of likely subclonal resistance; identifying other selective kinase inhibitors (or combination therapies) to  
421 which the mutant kinase is susceptible; supporting the selection of candidate molecules to advance to  
422 clinical trials based on anticipated activity against likely mutations; facilitating the enrollments of patients in  
423 mechanism-based basket trials; and generally augmenting the armamentarium of precision oncology.

## 424 Methods

### 425 System preparation

426 All system preparation utilized the Maestro Suite (Schrödinger) version 2016-4. Comparative modeling to add  
427 missing residues using a homologous template made use of the Splicer tool, while missing loops modeled

428 without a template used Prime. All tools employed default settings unless otherwise noted. The Abl wild-type  
429 sequence used in building all Abl kinase domain models utilized the ABL1\_HUMAN Isoform IA (P00519-1)  
430 UniProt gene sequence spanning S229-K512. Models were prepared in non-phosphorylated form. We used  
431 a residue indexing convention that places the Thr gatekeeper residue at position 315 to match common  
432 usage; an alternate indexing convention utilized in experimental X-ray structures for Abl:imatinib (PDB: 1OPJ)  
433 [59] and Abl:dasatinib (PDB: 4XEY) [60] was adjusted to match our convention.

434 **Complexes with co-crystal structures.** Chain B of the experimental structure of Abl:axitinib (PDB:  
435 4WA9) [44] was used, and four missing residues at the N- and C-termini were added using homology  
436 modeling with PDB 3IK3 [61] as the template following alignment of the respective termini of the kinase  
437 domain. Chain B was selected because chain A was missing an additional 3 and 4 residues at the N- and  
438 C-termini, respectively, in addition to 3- and 20-residue loops, both of which were resolved in chain B. All  
439 missing side chains were added with Prime. The co-crystal structure of Abl:bosutinib (PDB: 3UE4) [62] was  
440 missing 4 and 10 N- and C-terminal residues respectively in chain A that were built using homology modeling  
441 with 3IK3 as the template. All loops were resolved in chain A (chain B was missing two residues in the P-loop,  
442 Q252 and Y253). All missing side chains were added with Prime. The co-crystal structure of Abl:dasatinib  
443 (PDB: 4XEY) [60] was missing 2 and 9 N- and C-terminal residues, respectively, that were built via homology  
444 modeling using 3IK3 as the template. A 3 residue loop was absent in chain B but present in chain A; chain  
445 A was chosen. The co-crystal structure of Abl:imatinib (PDB: 1OPJ) [59] had no missing loops. Chain B was  
446 used because chain A was missing two C-terminal residues that were resolved in chain B. A serine was  
447 present at position 336 (index 355 in the PDB file) and was mutated to asparagine using Prime to match  
448 the human wild-type reference sequence (P00519-1). The co-crystal structure of Abl:nilotinib (PDB: 3CS9)  
449 [63] contained four chains in the asymmetric unit all of which were missing at least one loop. Chain A was  
450 selected because its one missing loop involved the fewest number of residues of the four chains; chain A  
451 was missing 4 and 12 N- and C-terminal residues, respectively, that were built using homology modeling  
452 with 3IK3 as the template. A 4-residue loop was missing in chain A (chain B and C were missing two loops,  
453 chain D was missing a five residue loop) that was built using Prime. The co-crystal structure of Abl:ponatinib  
454 (PDB: 3OXZ) [64] contained only one chain in the asymmetric unit. It had two missing loops, one 4 residues  
455 (built using Prime) and one 12 residues (built using homology modeling with 3OY3 [64] as the template).  
456 Serine was present at position 336 and was mutated to Asn using Prime to match the human wild-type  
457 reference sequence (P00519-1). Once the residue composition of the six Abl:TKI complexes were normalized  
458 to have the same sequence, the models were prepared using Protein Preparation Wizard. Bond orders  
459 were assigned using the Chemical Components Dictionary and hydrogen atoms were added. Missing side  
460 chain atoms were built using Prime. Termini were capped with N-acetyl (N-terminus) and N-methyl amide  
461 (C-terminus). If present, crystallographic water molecules were retained. Residue protonation states (e.g.  
462 Asp381 and Asp421) were determined using PROPKA [65] with a pH range of 5.0–9.0. Ligand protonation  
463 state was assigned using PROPKA with pH equal to the experimental assay. Hydrogen bonds were assigned  
464 by sampling the orientation of crystallographic water, Asn and Gln flips, and His protonation state. The  
465 positions of hydrogen atoms were minimized while constraining heavy atoms coordinates. Finally, restrained  
466 minimization of all atoms was performed in which a harmonic positional restraint (25.0 kcal/mol/Å<sup>2</sup>) was  
467 applied only to heavy atoms. *Table S9* summarizes the composition of the final models used for FEP.

468 **Complexes without co-crystal structures.** Co-crystal structures of Abl bound to erlotinib or gefitinib  
469 were not publicly available. To generate models of these complexes, Glide-SP [66] was utilized to dock  
470 these two compounds into an Abl receptor structure. Co-crystal structures of these two compounds bound  
471 to EGFR were publicly available and this information was used to obtain initial ligand geometries and to  
472 establish a reference binding mode against which our docking results could be structurally scored. The Abl  
473 receptor structure bound to bosutinib was used for docking because its structure was structurally similar to  
474 that of EGFR in the erlotinib- (PDB: 4HJO) [67] and gefitinib-bound (PDB: 4WKQ) [68] co-crystal structures.  
475 Abl was prepared for docking by using the Protein Preparation Wizard (PPW) with default parameters.  
476 Crystallographic waters were removed but their coordinates retained for a subsequent step in which they

were optionally reintroduced. Erlotinib and gefitinib protonation states at pH  $7.0 \pm 2.0$  were determined using Epik [69]. Docking was performed using the Glide-SP workflow. The receptor grid was centered on bosutinib. The backbone NH of Met318 was chosen to participate in a hydrogen bonding constraint with any hydrogen bond donor on the ligand. The hydroxyl of T315 was allowed to rotate in an otherwise rigid receptor. Ligand docking was performed with enhanced sampling; otherwise default settings were used. Epik state penalties were included in the scoring. The 16 highest ranked (Glide-SP score) poses were retained for subsequent scoring. To determine the docked pose that would be subsequently used for free energy calculations, the ligand heavy-atom RMSD between the 16 poses and the EGFR co-crystal structures (PDB IDs 4HJO and 4WKQ) was determined. The pose in which erlotinib or gefitinib most structurally resembled the EGFR co-crystal structure (lowest heavy-atom RMSD) was chosen as the pose for subsequent FEP+. Two sets of complex structures were subjected to free energy calculations to determine the effect of crystal waters: In the first set, without crystallographic waters, the complexes were prepared using Protein Prep Wizard as above. In the second set, the crystallographic waters removed prior to docking were added back, and waters in the binding pocket that clashed with the ligand were removed.

#### 491 Force field parameter assignment

492 The OPLS3 forcefield [25] version that shipped with Schrödinger Suite release 2016-4 was used to parameterize the protein and ligand. Torsion parameter coverage was checked for all ligand fragments using Force Field Builder. The two ligands that contained a fragment with a torsion parameter not covered by OPLS3 495 were axitinib and bosutinib; Force Field Builder was used to obtain these parameters. SPC parameters [70] 496 were used for water. For mutations that change the net charge of the system, counterions were included to 497 neutralize the system with additional Na<sup>+</sup> and Cl<sup>-</sup> ions added to achieve 0.15 M excess to mimic the solution 498 conditions of the experimental assay.

#### 499 Prime (MM-GBSA)

500 Prime was used to predict the geometry of mutant side chains and to calculate relative changes in free energy 501 using MM-GBSA single-point estimates [39]. VSGB [71] was used as the implicit solvent model to calculate 502 the solvation free energies for the four states (complex/wild-type, complex/mutant, apo protein/wild-type, 503 and apo protein/mutant) and  $\Delta\Delta G$  calculated using the thermodynamic cycle depicted in **Figure 1b**. Unlike 504 FEP (see below), which simulates the horizontal legs of the thermodynamic cycle, MM-GBSA models the 505 vertical legs by computing the interaction energy between the ligand and protein in both wild-type and 506 mutant states, subtracting these to obtain the  $\Delta\Delta G$  of mutation on the binding free energy.

#### 507 Alchemical free energy perturbation calculations using FEP+

508 Alchemical free energy calculations were performed using the FEP+ tool in the Schrödinger Suite version 509 2016-4, which offers a fully automated workflow requiring only an input structure (wild-type complex) and 510 specification of the desired mutation. The default protocol was used throughout: It assigns protein and 511 ligand force field parameters (as above), generates a dual-topology [72] alchemical system for transforming 512 wild-type into mutant protein (whose initial structure is modeled using Prime), generates the solvent-leg 513 endpoints (wild-type and mutant apo protein), and constructs intermediate windows spanning wild-type 514 and mutant states. Simulations of the apo protein were setup by removing the ligand from the prepared 515 complex (see System Preparation) followed by an identical simulation protocol as that used for the complex. 516 Charge-conserving mutations utilized 12  $\lambda$  windows (24 systems) while charge-changing mutations utilized 24 517  $\lambda$  windows (48 systems). Each system was solvated in an orthogonal box of explicit solvent (SPC water [70]) 518 with box size determined to ensure that solute atoms were no less than 5 Å (complex leg) or 10 Å (solvent leg) 519 from an edge of the box. For mutations that change the net charge of the system, counterions were included 520 to neutralize the charge of the system, and additional Na<sup>+</sup> and Cl<sup>-</sup> ions added to achieve 0.15 M excess 521 NaCl to mimic the solution conditions of the experimental assay. The artifact in electrostatic interactions for 522 charge change perturbations due to periodic boundary conditions in MD simulations are corrected based on 523 the method proposed by Rocklin *et al.* [73].

524 System equilibration was automated. It followed the default 5-stage Desmond protocol: (i) 100 ps with 525 1 fs time steps of Brownian dynamics with positional restraints of solute heavy atoms to their initial geometry

526 using a restraint force constant of 50 kcal/mol/Å<sup>2</sup>; this Brownian dynamics integrator corresponds to a  
527 Langevin integrator in the limit when  $\tau \rightarrow 0$ , modified to stabilize equilibration of starting configurations  
528 with high potential energies; particle and piston velocities were clipped so that particle displacements were  
529 limited to 0.1 Å, in any direction. (ii) 12 ps MD simulations with 1 fs time step using Langevin thermostat at  
530 10 K with constant volume, using the same restraints; (iii) 12 ps MD simulations with 1 fs time step using  
531 Langevin thermostat and barostat [74] at 10 K and constant pressure of 1 atmosphere, using the same  
532 restraints; (iv) 12 ps MD simulations with 1 fs time step using Langevin thermostat and barostat at 300 K  
533 and constant pressure of 1 atmosphere, using the same restraints; (v) a final unrestrained equilibration  
534 MD simulation of 240 ps with 2 fs time step using Langevin thermostat and barostat at 300 K and constant  
535 pressure of 1 atmosphere. Electrostatic interactions were computed with particle-mesh Ewald (PME) [75]  
536 and a 9 Å cutoff distance was used for van de Waals interactions. The production MD simulation was  
537 performed in the NPT ensemble using the MTK method [76] with integration time steps of 4 fs, 4 fs, and 8 fs  
538 respectively for the bonded, near, and far interactions following the RESPA method [77] through hydrogen  
539 mass repartitioning [78]. Production FEP+ calculations utilized Hamiltonian replica exchange with solute  
540 tempering (REST) [79], with automated definition of the REST region. Dynamics were performed with  
541 constant pressure of 1 atmosphere and constant temperature of 300 K for 5 ns in which exchanges between  
542 windows was attempted every 1.2 ps.

543 Because cycle closure could not be used to reduce statistical errors via path redundancy [79], we  
544 instead performed mutational free energy calculations in triplicate by initializing dynamics with different  
545 random seeds. The relative free energies for each mutation in each independent run were calculated using  
546 BAR [80, 81] The reported  $\Delta\Delta G$  was computed as the mean of the computed  $\Delta\Delta G$  from three independent  
547 simulations. Triplicate simulations were performed in parallel using four NVIDA Pascal Architecture GPUs  
548 per alchemical free-energy simulation (12 GPUs in total), requiring ~6 hours in total to compute  $\Delta\Delta G$ .

#### 549 Obtaining $\Delta\Delta G$ from $\Delta\text{pIC}_{50}$ benchmark set data

550 Reference relative free energies were obtained from three publicly available sources of  $\Delta\text{pIC}_{50}$  data (**Table 1**).  
551 Under the assumption of Michaelis-Menten binding kinetics (pseudo first-order, but relative free energies are  
552 likely consistent), the inhibitor is competitive with ATP (**Equation 1**). This assumption has been successfully  
553 used to estimate relative free energies [37, 82-84] using the relationship between  $\text{IC}_{50}$  and competitive  
554 inhibitor affinity  $K_i$ ,

$$\text{IC}_{50} = \frac{K_i}{1 + \frac{[S_0]}{K_M}}. \quad (1)$$

555 If the Michaelis constant for ATP ( $K_M$ ) is much larger than the initial ATP concentration  $S_0$ , the relation in  
556 **Equation 1** will tend towards the equality  $\text{IC}_{50} = K_i$ . The relative change in binding free energy of Abl:TKI  
557 binding due to protein mutation is simply,

$$\Delta\Delta G = -RT \ln \frac{\text{IC}_{50,WT}}{\text{IC}_{50,mut}} \quad (2)$$

558 where  $\text{IC}_{50,WT}$  is the  $\text{IC}_{50}$  value for the TKI binding to the wild-type protein and  $\text{IC}_{50,mut}$  is the  $\text{IC}_{50}$  value for the  
559 mutant protein.  $R$  is the ideal gas constant and  $T$  is taken to be room temperature (300 K).

560 As alluded to above, relating  $\Delta\text{pIC}_{50}$ s to  $\Delta\Delta G$ s assumes that the Michaelis constant for ATP is much larger  
561 than the initial concentration of ATP, and that the experimentally observed  $\Delta\text{pIC}_{50}$  change is solely from  
562 changes in kinase:TKI binding affinity. In practice, not all of these assumptions may hold. For example, the  
563 experimentally observed  $\Delta\text{pIC}_{50}$  might depend on the metabolism of drugs, and for drugs with different  
564 mechanisms of action than directly binding to the kinase binding pocket (e.g., binding to the transition  
565 structures of kinases, target gene amplification, up-/down-regulation of positive-/negative-feedback effectors,  
566 diminished synergism of pro-apoptotic machinery, decoupling of the target from cell survival circuits) [85, 86],  
567 their inhibition ability might not correlate well with binding affinity. However, the comparison between  
568  $\Delta\text{pIC}_{50}$  and  $\Delta K_D$  is presented in **Figure 2d**, and this comparison indicates the assumptions we used to relate  
569  $\Delta\text{pIC}_{50}$  to  $\Delta\Delta G$  are reasonable for the dataset we studied.

570 **Assessing prediction performance**

571 Quantitative accuracy metrics

572 Mean unsigned error (MUE) was calculated by taking the average absolute difference between predicted and  
573 experimental estimates of  $\Delta\Delta G$ . Root-mean square error (RMSE) was calculated by taking the square root  
574 of the average squared difference between predicted and experimental estimates of  $\Delta\Delta G$ . MUE depends  
575 linearly on errors such that large and small errors contribute equally to the average value, while RMSE  
576 depends quadratically on errors, magnifying their effect on the average value.

577 Truth tables

578 Two-class truth tables were constructed to characterize the ability of Prime and FEP+ to correctly classify  
579 mutations as susceptible ( $\Delta\Delta G \leq 1.36$  kcal/mol) or resistant ( $\Delta\Delta G > 1.36$  kcal/mol), where the 1.36 kcal/mol  
580 threshold represents a 10-fold change in affinity. Accuracy was calculated as the fraction of all predictions  
581 that were correctly classified as sensitizing, neutral, or resistant. Sensitivity and specificity were calculated  
582 using a binary classification of resistant ( $\Delta\Delta G > 1.36$  kcal/mol) or susceptible ( $\Delta\Delta G \leq 1.36$  kcal/mol). Specificity  
583 was calculated as the fraction of correctly predicted non-resistant mutations out of all truly susceptible  
584 mutations **S**. Sensitivity was calculated as the fraction of correctly predicted resistant mutations out of all  
585 truly resistant mutations, **R**. The number of susceptible mutations was 113 for axitinib, bosutinib, dasatinib,  
586 imatinib, nilotinib and ponatinib, and 12 for erlotinib and gefitinib; the number of resistant mutations **R** was  
587 18 for axitinib, bosutinib, dasatinib, imatinib, nilotinib, and ponatinib, and 1 for erlotinib and gefitinib.

588 Consensus model

589 First, Prime and FEP+ (n=142) were scaled by minimizing their RMSE to experiment by optimizing slope using  
590 linear regression. The resulting (minimum) RMSE was used in a subsequent step to combine the scaled FEP+  
591 and scaled Prime free energies with inverse-variance weighted averaging.

592 ROC

593 A ROC curve was generated by computing the true positive rate (sensitivity) and the true negative rate  
594 (specificity) when the classification cutoff differentiating resistant from sensitizing mutations is changed for  
595 (only) the predicted values of  $\Delta\Delta G$ . Cutoffs were chosen by taking the minimum and maximum value of  $\Delta\Delta G$   
596 for a data set (Prime or FEP+), and iteratively computing specificity and sensitivity in steps of 0.001 kcal/mol,  
597 which by this definition will be in the range [0,1]. Experimental positives and negatives were classified with  
598 the 1.36 kcal/mol cutoff. ROC-AUC was computed using the trapezoidal rule.

599 Estimating uncertainties of physical-modeling results

600 95% symmetric confidence intervals (CI, 95%) for all performance metrics were calculated using bootstrap by  
601 resampling all datasets with replacement, with 1000 resampling events. Confidence intervals were estimated  
602 for all performance metrics and reported as  $x_{x_{\text{low}}}^{x_{\text{high}}}$  where  $x$  is the mean statistic calculated from the complete  
603 dataset (e.g. RMSE), and  $x_{\text{low}}$  and  $x_{\text{high}}$  are the values of the statistic at the 2.5<sup>th</sup> and 97.5<sup>th</sup> percentiles of the  
604 value-sorted list of the bootstrap samples. Uncertainty for  $\Delta\Delta G$ s was computed by the standard deviation  
605 between three independent runs (using different random seeds to set initial velocities), where the 95% CI  
606 was  $[\Delta\Delta G - 1.96 \times \sigma_{\text{FEP+}}, \Delta\Delta G + 1.96 \times \sigma_{\text{FEP+}}]$  kcal/mol.  $1\sigma$  used in plots for FEP+ and experiment;  $0\sigma$  for Prime.

607 Bayesian hierarchical model to estimate intrinsic error

608 We used Bayesian inference to estimate the true underlying prediction error of Prime and FEP+ by making  
609 use of known properties of the experimental variability (characterized in **Figure 2**) and statistical uncertainty  
610 estimates generated by our calculations under weak assumptions about the character of the error.

611 We presume the true free energy differences of mutation  $i$ ,  $\Delta\Delta G_i^{\text{true}}$ , comes from a normal background  
612 distribution of unknown mean and variance,

$$\Delta\Delta G_i^{\text{true}} \sim \mathcal{N}(\mu_{\text{mut}}, \sigma_{\text{mut}}^2) \quad i = 1, \dots, M \quad (3)$$

613 where there are  $M$  mutations in our dataset. We assign weak priors to the mean and variance

$$\mu_{\text{mut}} \sim U(-6, +6) \quad (4)$$

$$\sigma_{\text{mut}} \propto 1 \quad (5)$$

614 where we limit  $\sigma > 0$ .

615 We presume the true computational predictions (absent statistical error) differ from the (unknown)  
 616 true free energy difference of mutation  $\Delta\Delta G_i^{\text{true}}$  by normally-distributed errors with zero bias but standard  
 617 deviation equal to the RMSE for either Prime or FEP+, the quantity we are focused on estimating:

$$\Delta\Delta G_{i,\text{Prime}}^{\text{true}} \sim \mathcal{N}(\Delta\Delta G_i^{\text{true}}, \text{RMSE}_{\text{Prime}}^2) \quad (6)$$

$$\Delta\Delta G_{i,\text{FEP+}}^{\text{true}} \sim \mathcal{N}(\Delta\Delta G_i^{\text{true}}, \text{RMSE}_{\text{FEP+}}^2) \quad (7)$$

618 In the case of Prime, since the computation is deterministic, we actually calculate  $\Delta\Delta G_{i,\text{Prime}}^{\text{true}}$  for each  
 619 mutant. For FEP+, however, the computed free energy changes are corrupted by statistical error, which we  
 620 also presume to be normally distributed with standard deviation  $\sigma_{\text{calc},i}$ ,

$$\Delta\Delta G_{i,\text{FEP+}} \sim \mathcal{N}(\Delta\Delta G_{i,\text{FEP+}}, \sigma_{i,\text{FEP+}}^2) \quad (8)$$

621 where  $\Delta\Delta G_{i,\text{FEP+}}$  is the free energy computed for mutant  $i$  by FEP+, and  $\sigma_{i,\text{FEP+}}$  is the corresponding statistical  
 622 error estimate.

623 The experimental data we observe is also corrupted by error, which we presume to be normally dis-  
 624 tributed with standard deviation  $\sigma_{\text{exp}}$ :

$$\Delta\Delta G_{i,\text{exp}} \sim \mathcal{N}(\Delta\Delta G_i, \sigma_{\text{exp}}^2) \quad (9)$$

625 Here, we used an estimate of  $K_d$ - and IC<sub>50</sub>-derived  $\Delta\Delta G$  variation derived from the empirical RMSE of 0.81  
 626 kcal/mol, where we took  $\sigma_{\text{exp}} \approx 0.81/\sqrt{2} = 0.57$  kcal/mol to ensure the difference between two random  
 627 measurements of the same mutant would have an empirical RMSE of 0.81 kcal/mol.

628 Under the assumption that the true  $\Delta\Delta G$  is normally distributed and the calculated value differs from  
 629 the true value via a normal error model, it can easily be shown that the MUE is related to the RMSE via

$$\text{MUE} = \int dx_{\text{true}} p(x_{\text{true}}) \int dx_{\text{calc}} p(x_{\text{calc}}|x_{\text{true}}) |x_{\text{calc}} - x_{\text{true}}| \quad (10)$$

$$= \int dx_{\text{true}} \frac{1}{\sqrt{2\pi\sigma_{\text{true}}^2}} e^{-\frac{(x_{\text{true}}-\mu_{\text{true}})^2}{2\sigma_{\text{true}}^2}} \int dx_{\text{calc}} \frac{1}{\sqrt{2\pi\sigma_{\text{calc}}^2}} e^{-\frac{(x_{\text{calc}}-\mu_{\text{true}})^2}{2\sigma_{\text{calc}}^2}} |x_{\text{calc}} - x_{\text{true}}| \quad (11)$$

$$= \sqrt{\frac{2}{\pi}} \text{RMSE} \quad (12)$$

630 The model was implemented using PyMC3 [87], observable quantities were set to their computed or  
 631 experimental values, and 5000 samples drawn from the posterior (after discarding an initial 500 samples to  
 632 burn-in) using the default NUTS sampler. Expectations and posterior predictive intervals were computed  
 633 from the marginal distributions obtained from the resulting traces.

### 634 Data availability

635 Compiled experimental datasets, input files for Prime and FEP+ and computational results can be found at  
 636 the following URL: <https://goo.gl/6cC8Bu>

### 637 Code availability

638 Scripts used for statistics analysis (including the Bayesian inference model) can be found at the following  
 639 URL: <https://goo.gl/6cC8Bu>

## 640 Acknowledgments

641 We thank Daniel Robinson (Schrödinger), Sonya M. Hanson (MSKCC), and Gregory A. Ross (MSKCC) for helpful  
642 discussions. JDC acknowledges support from NIH National Cancer Institute Cancer Center Core Grant P30  
643 CA008748; JDC and SKA acknowledge support from the Sloan Kettering Institute, Cycle for Survival, and NIH  
644 grant R01 GM121505. KH acknowledges help from Wei Chen (Schrödinger) and Anthony Clark (Schrödinger)  
645 for instructions on running mutations changing the net charge of the system, and Simon Gao (Schrödinger)  
646 for assistance in computational resources.

## 647 Disclosures

648 JDC is a member of the Scientific Advisory Board for Schrödinger Inc.

## 649 Author Contributions

650 KH, JDC, CN, RA, and LW designed the research; KH, SA, TS, and LW identified experimental datasets; KH and  
651 LW performed the simulations; KH, CN, SKA, SR, TS, RA, JDC, and LW analyzed the data; KH, JDC, SKA, and LW  
652 wrote the paper.

## 653 References

- 654 [1] Robert Roskoski Jr. USFDA Approved Protein Kinase Inhibitors. . 2017; <http://www.brimr.org/PKI/PKIs.htm>, updated  
655 3 May 2017.
- 656 [2] Santos R, Ursu O, Gaulton A, Bento AP, Donadi RS, Bologa CG, Karlsson A, Al-Lazikani B, Hersey A, Oprea TI,  
657 Overington JP. A Comprehensive Map of Molecular Drug Targets. *Nat Rev Drug Discov.* 2016 Dec; 16(1):19–34. doi:  
658 [10.1038/nrd.2016.230](https://doi.org/10.1038/nrd.2016.230).
- 659 [3] Shah NP, Nicoll JM, Nagar B, Gorre ME, Paquette RL, Kuriyan J, Sawyers CL. Multiple BCR-ABL Kinase Domain  
660 Mutations Confer Polyclonal Resistance to the Tyrosine Kinase Inhibitor Imatinib (ST1571) in Chronic Phase and Blast  
661 Crisis Chronic Myeloid Leukemia. *Cancer Cell.* 2002 Aug; 2(2):117–125.
- 662 [4] Buczek M, Escudier B, Bartnik E, Szczylik C, Czarnecka A. Resistance to tyrosine kinase inhibitors in clear cell  
663 renal cell carcinoma: From the patient's bed to molecular mechanisms. *Biochimica et Biophysica Acta (BBA) -*  
664 *Reviews on Cancer.* 2014; 1845(1):31 – 41. <http://www.sciencedirect.com/science/article/pii/S0304419X13000437>, doi:  
665 <https://doi.org/10.1016/j.bbcan.2013.10.001>.
- 666 [5] Huang L, Fu L. Mechanisms of Resistance to EGFR Tyrosine Kinase Inhibitors. *Acta Pharm Sin B.* 2015; 5(5):390–401.
- 667 [6] Meyer SC, Levine RL. Molecular Pathways: Molecular Basis for Sensitivity and Resistance to JAK Kinase Inhibitors.  
668 *Clin Cancer Res.* 2014; 20(8):2051–2059. doi: [10.1158/1078-0432.CCR-13-0279](https://doi.org/10.1158/1078-0432.CCR-13-0279).
- 669 [7] Davare MA, Vellore NA, Wagner JP, Eide CA, Goodman JR, Drilon A, Deininger MW, O'Hare T, Druker BJ. Structural  
670 Insight into Selectivity and Resistance Profiles of ROS1 Tyrosine Kinase Inhibitors. *Proc Natl Acad Sci.* 2015;  
671 112(39):E5381–E5390. doi: [10.1073/pnas.1515281112](https://doi.org/10.1073/pnas.1515281112).
- 672 [8] Van Allen EM, Wagle N, Sucker A, Treacy DJ, Johannessen CM, Goetz EM, Place CS, Taylor-Weiner A, Whittaker S,  
673 Kryukov GV, Hodis E, Rosenberg M, McKenna A, Cibulskis K, Farlow D, Zimmer L, Hillen U, Gutzmer R, Goldinger SM,  
674 Uigurel S, et al. The Genetic Landscape of Clinical Resistance to RAF Inhibition in Metastatic Melanoma. *Cancer Discov.*  
675 2014; 4(1):94–109. doi: [10.1158/2159-8290.CD-13-0617](https://doi.org/10.1158/2159-8290.CD-13-0617).
- 676 [9] Rani S, Corcoran C, Shiels L, Germano S, Breslin S, Madden S, McDermott MS, Browne BC, OtextquoterightDonovan  
677 N, Crown J, Gogarty M, Byrne AT, OtextquoterightDriscoll L. Neuromedin U: A Candidate Biomarker and Therapeutic  
678 Target to Predict and Overcome Resistance to HER-Tyrosine Kinase Inhibitors. *Cancer Res.* 2014; 74(14):3821–3833.  
679 doi: [10.1158/0008-5472.CAN-13-2053](https://doi.org/10.1158/0008-5472.CAN-13-2053).
- 680 [10] Holohan C, Van Schaeybroeck S, Longley DB, Johnston PG. Cancer Drug Resistance: An Evolving Paradigm. *Nat Rev  
681 Cancer.* 2013 Sep; 13(10):714–726. doi: [10.1038/nrc3599](https://doi.org/10.1038/nrc3599).
- 682 [11] Weisberg E, Manley PW, Cowan-Jacob SW, Hochhaus A, Griffin JD. Second Generation Inhibitors of BCR-ABL for  
683 the Treatment of Imatinib-Resistant Chronic Myeloid Leukaemia. *Nat Rev Cancer.* 2007 May; 7(5):345–356. doi:  
684 [10.1038/nrc2126](https://doi.org/10.1038/nrc2126).
- 685 [12] Y Lu X, Cai Q, Ding K. Recent Developments in the Third Generation Inhibitors of Bcr-Abl for Overriding T315I  
686 Mutation. *Curr Med Chem.* 2011 May; 18(14):2146–2157. doi: [10.2174/092986711795656135](https://doi.org/10.2174/092986711795656135).

687 [13] **Juchum M**, Günther M, Laufer SA. Fighting Cancer Drug Resistance: Opportunities and Challenges for Mutation-  
688 Specific EGFR Inhibitors. *Drug Resist Updat*. 2015 May; 20:12–28. doi: [10.1016/j.drup.2015.05.002](https://doi.org/10.1016/j.drup.2015.05.002).

689 [14] **Song Z**, Wang M, Zhang A. Alectinib: A Novel Second Generation Anaplastic Lymphoma Kinase (ALK) Inhibitor for  
690 Overcoming Clinically-Acquired Resistance. *Acta Pharm Sin B*. 2015 Jan; 5(1):34–37. doi: [10.1016/j.apsb.2014.12.007](https://doi.org/10.1016/j.apsb.2014.12.007).

691 [15] **Neel DS**, Bivona TG. Resistance Is Futile: Overcoming Resistance to Targeted Therapies in Lung Adenocarcinoma.  
692 *Npj Precis Oncol*. 2017 Dec; 1(1). doi: [10.1038/s41698-017-0007-0](https://doi.org/10.1038/s41698-017-0007-0).

693 [16] **Gruber F**, Hjorth-Hansen H, Mikkola I, Stenke L, TA J. A Novel BCR-ABL Splice Isoform Is Associated with the L248V  
694 Mutation in CML Patients with Acquired Resistance to Imatinib. *Leuk Off J Leuk Soc Am Leuk Res Fund UK*. 2006 Dec;  
695 20:2057–60.

696 [17] **Chandarlapaty S**, Sawai A, Scaltriti M, Rodrik-Outmezguine V, Grbovic-Huezo O, Serra V, Majumder PK, Baselga J,  
697 Rosen N. AKT Inhibition Relieves Feedback Suppression of Receptor Tyrosine Kinase Expression and Activity. *Cancer Cell*. 2011 Jan; 19(1):58–71. doi: [10.1016/j.ccr.2010.10.031](https://doi.org/10.1016/j.ccr.2010.10.031).

698 [18] **Knight ZA**, Lin H, Shokat KM. Targeting the Cancer Kinome through Polypharmacology. *Nat Rev Cancer*. 2010;  
699 10(2):130.

700 [19] **Housman G**, Byler S, Heerboth S, Lapinska K, Longacre M, Snyder N, Sarkar S. Drug Resistance in Cancer: An  
701 Overview. *Cancers*. 2014 Sep; 6(3):1769–1792. doi: [10.3390/cancers6031769](https://doi.org/10.3390/cancers6031769).

702 [20] **Zehir A**, Benayed R, Shah RH, Syed A, Middha S, Kim HR, Srinivasan P, Gao J, Chakravarty D, Devlin SM, Hellmann MD,  
703 Barron DA, Schram AM, Hameed M, Dogan S, Ross DS, Hechtman JF, DeLair DF, Yao J, Mandelker DL, et al. Mutational  
704 Landscape of Metastatic Cancer Revealed from Prospective Clinical Sequencing of 10,000 Patients. *Nat Med*. 2017  
705 May; 23(6):703–713. doi: [10.1038/nm.4333](https://doi.org/10.1038/nm.4333).

706 [21] **Redig AJ**, Jänne PA. Basket Trials and the Evolution of Clinical Trial Design in an Era of Genomic Medicine. *American  
707 Society of Clinical Oncology*; 2015.

708 [22] **Hyman DM**, Taylor BS, Baselga J. Implementing Genome-Driven Oncology. *Cell*. 2017 Feb; 168(4):584–599. doi:  
709 [10.1016/j.cell.2016.12.015](https://doi.org/10.1016/j.cell.2016.12.015).

710 [23] **Pesesky MW**, Hussain T, Wallace M, Patel S, Andleeb S, Burnham CAD, Dantas G. Evaluation of Machine Learning  
711 and Rules-Based Approaches for Predicting Antimicrobial Resistance Profiles in Gram-Negative Bacilli from Whole  
712 Genome Sequence Data. *Front Microbiol*. 2016 Nov; 7. doi: [10.3389/fmicb.2016.01887](https://doi.org/10.3389/fmicb.2016.01887).

713 [24] **Melnikov A**, Rogov P, Wang L, Gnrke A, Mikkelsen TS. Comprehensive Mutational Scanning of a Kinase *in Vivo* Reveals  
714 Substrate-Dependent Fitness Landscapes. *Nucleic Acids Res*. 2014 Aug; 42(14):e112–e112. doi: [10.1093/nar/gku511](https://doi.org/10.1093/nar/gku511).

715 [25] **Harder E**, Damm W, Maple J, Wu C, Reboul M, Xiang JY, Wang L, Lupyan D, Dahlgren MK, Knight JL, Kaus JW, Cerutti  
716 DS, Krilov G, Jorgensen WL, Abel R, Friesner RA. OPLS3: A Force Field Providing Broad Coverage of Drug-like Small  
717 Molecules and Proteins. *J Chem Theory Comput*. 2016 Jan; 12(1):281–296. doi: [10.1021/acs.jctc.5b00864](https://doi.org/10.1021/acs.jctc.5b00864).

718 [26] **Huang J**, MacKerell AD. CHARMM36 All-Atom Additive Protein Force Field: Validation Based on Comparison to NMR  
719 Data. *J Comput Chem*. 2013 Sep; 34(25):2135–2145. doi: [10.1002/jcc.23354](https://doi.org/10.1002/jcc.23354).

720 [27] **Maier JA**, Martinez C, Kasavajhala K, Wickstrom L, Hauser KE, Simmerling C. ff14SB: Improving the Accuracy of  
721 Protein Side Chain and Backbone Parameters from ff99SB. *J Chem Theory Comput*. 2015 Aug; 11(8):3696–3713. doi:  
722 [10.1021/acs.jctc.5b00255](https://doi.org/10.1021/acs.jctc.5b00255).

723 [28] **Chodera JD**, Mobley DL, Shirts MR, Dixon RW, Branson K, Pande VS. Alchemical Free Energy Methods for Drug  
724 Discovery: Progress and Challenges. *Curr Opin Struct Biol*. 2011 Apr; 21(2):150–160. doi: [10.1016/j.sbi.2011.01.011](https://doi.org/10.1016/j.sbi.2011.01.011).

725 [29] **Wang L**, Wu Y, Deng Y, Kim B, Pierce L, Krilov G, Lupyan D, Robinson S, Dahlgren MK, Greenwood J, Romero DL, Masse  
726 C, Knight JL, Steinbrecher T, Beuming T, Damm W, Harder E, Sherman W, Brewer M, Wester R, et al. Accurate and  
727 Reliable Prediction of Relative Ligand Binding Potency in Prospective Drug Discovery by Way of a Modern Free-Energy  
728 Calculation Protocol and Force Field. *J Am Chem Soc*. 2015 Feb; 137(7):2695–2703. doi: [10.1021/ja512751q](https://doi.org/10.1021/ja512751q).

729 [30] **Abel R**, Mondal S, Masse C, Greenwood J, Harriman G, Ashwell MA, Bhat S, Wester R, Frye L, Kapeller R, et al.  
730 Accelerating drug discovery through tight integration of expert molecular design and predictive scoring. *Current  
731 opinion in structural biology*. 2017; 43:38–44.

732 [31] **Aldeghi M**, Heifetz A, Bodkin MJ, Knapp S, Biggin PC. Accurate Calculation of the Absolute Free Energy of Binding for  
733 Drug Molecules. *Chem Sci*. 2016; 7(1):207–218. doi: [10.1039/C5SC02678D](https://doi.org/10.1039/C5SC02678D).

735 [32] **Cappel D**, Hall ML, Lenselink EB, Beuming T, Qi J, Bradner J, Sherman W. Relative Binding Free Energy Calculations  
736 Applied to Protein Homology Models. *J Chem Inf Model*. 2016; 56(12):2388–2400. doi: [10.1021/acs.jcim.6b00362](https://doi.org/10.1021/acs.jcim.6b00362).

737 [33] **Clark AJ**, Gindin T, Zhang B, Wang L, Abel R, Murret CS, Xu F, Bao A, Lu NJ, Zhou T, et al. Free Energy Perturbation  
738 Calculation of Relative Binding Free Energy between Broadly Neutralizing Antibodies and the gp120 Glycoprotein of  
739 HIV-1. *Journal of molecular biology*. 2017; 429(7):930–947.

740 [34] **Steinbrecher T**, Zhu C, Wang L, Abel R, Negron C, Pearlman D, Feyfant E, Duan J, Sherman W. Predicting the Effect of  
741 Amino Acid Single-Point Mutations on Protein Stability—Large-Scale Validation of MD-Based Relative Free Energy  
742 Calculations. *Journal of molecular biology*. 2017; 429(7):948–963.

743 [35] **Ford MC**, Babaoglu K. Examining the Feasibility of Using Free Energy Perturbation (FEP+) in Predicting Protein  
744 Stability. *J Chem Inf Model*. 2017 Jun; 57(6):1276–1285. doi: [10.1021/acs.jcim.7b00002](https://doi.org/10.1021/acs.jcim.7b00002).

745 [36] **Zou J**, Song B, Simmerling C, Raleigh D. Experimental and Computational Analysis of Protein Stabilization by Gly-  
746 to- D -Ala Substitution: A Convolution of Native State and Unfolded State Effects. *J Am Chem Soc*. 2016 Dec;  
747 138(48):15682–15689. doi: [10.1021/jacs.6b09511](https://doi.org/10.1021/jacs.6b09511).

748 [37] **Mondal J**, Tiwary P, Berne BJ. How a Kinase Inhibitor Withstands Gatekeeper Residue Mutations. *J Am Chem Soc*.  
749 2016; 138(13):4608–4615. doi: [10.1021/jacs.6b01232](https://doi.org/10.1021/jacs.6b01232).

750 [38] **Lovering F**, Aevazelis C, Chang J, Dehnhardt C, Fitz L, Han S, Janz K, Lee J, Kaila N, McDonald J, Moore W, Moretto  
751 A, Papaioannou N, Richard D, Ryan MS, Wan ZK, Thorarensen A. Imidazotriazines: Spleen Tyrosine Kinase  
752 (Syk) Inhibitors Identified by Free-Energy Perturbation (FEP). *ChemMedChem*. 2016 Jan; 11(2):217–233. doi:  
753 [10.1002/cmdc.201500333](https://doi.org/10.1002/cmdc.201500333).

754 [39] **Rapp C**, Kalyanaraman C, Schiffmiller A, Schoenbrun EL, Jacobson MP. A Molecular Mechanics Approach to Modeling  
755 Protein–Ligand Interactions: Relative Binding Affinities in Congeneric Series. *J Chem Inf Model*. 2011 Sep; 51(9):2082–  
756 2089. doi: [10.1021/ci200033n](https://doi.org/10.1021/ci200033n).

757 [40] **Shirts MR**, Mobley DL, Chodera JD. Chapter 4 Alchemical Free Energy Calculations: Ready for Prime Time? In: *Annual  
758 Reports in Computational Chemistry*, vol. 3 Elsevier; 2007.p. 41–59.

759 [41] **Mobley DL**, Klimovich PV. Perspective: Alchemical Free Energy Calculations for Drug Discovery. *J Chem Phys*. 2012  
760 Dec; 137(23):230901. doi: [10.1063/1.4769292](https://doi.org/10.1063/1.4769292).

761 [42] **Abel R**, Mondal S, Masse C, Greenwood J, Harriman G, Ashwell MA, Bhat S, Wester R, Frye L, Kapeller R, Friesner RA.  
762 Accelerating Drug Discovery through Tight Integration of Expert Molecular Design and Predictive Scoring. *Curr Opin  
763 Struct Biol*. 2017 Apr; 43:38–44. doi: [10.1016/j.sbi.2016.10.007](https://doi.org/10.1016/j.sbi.2016.10.007).

764 [43] **Kuhn B**, Tichý M, Wang L, Robinson S, Martin RE, Kuglstaetter A, Benz J, Giroud M, Schirmeister T, Abel R, Diederich F,  
765 Hert J. Prospective Evaluation of Free Energy Calculations for the Prioritization of Cathepsin L Inhibitors. *J Med Chem*.  
766 2017 Mar; 60(6):2485–2497. doi: [10.1021/acs.jmedchem.6b01881](https://doi.org/10.1021/acs.jmedchem.6b01881).

767 [44] **Pemovska T**, Johnson E, Kontro M, Repasky GA, Chen J, Wells P, Cronin CN, McTigue M, Kallioniemi O, Porkka K,  
768 Murray BW, Wennerberg K. Axitinib Effectively Inhibits BCR-ABL1(T315I) with a Distinct Binding Conformation. *Nature*.  
769 2015 Feb; 519(7541):102–105. doi: [10.1038/nature14119](https://doi.org/10.1038/nature14119).

770 [45] **Schrock A**, Chen TH, Clackson T, Rivera VM. Comprehensive Analysis Of The In Vitro Potency Of Ponatinib, and  
771 All Other Approved BCR-ABL Tyrosine Kinase Inhibitors (TKIs), Against A Panel Of Single And Compound BCR-ABL  
772 Mutants. *Blood*. 2013; 122(21):3992–3992.

773 [46] **Davis MI**, Hunt JP, Herrgard S, Ciceri P, Wodicka LM, Pallares G, Hocker M, Treiber DK, Zarrinkar PP. Comprehensive  
774 Analysis of Kinase Inhibitor Selectivity. *Nat Biotechnol*. 2011 Oct; 29(11):1046–1051. doi: [10.1038/nbt.1990](https://doi.org/10.1038/nbt.1990).

775 [47] **Soverini S**, Colarossi S, Gnani A, Rosti G, Castagnetti F, Poerio A, Iacobucci I, Amabile M, Abruzzese E, Orlandi  
776 E, Radaelli F, Ciccone F, Tiribelli M, di Lorenzo R, Caracciolo C, Izzo B, Pane F, Saglio G, Baccarani M, Martinelli G.  
777 Contribution of ABL Kinase Domain Mutations to Imatinib Resistance in Different Subsets of Philadelphia-Positive  
778 Patients: By the GIMEMA Working Party on Chronic Myeloid Leukemia. *Clinical Cancer Research*. 2006; 12(24):7374–  
779 7379. <http://clincancerres.aacrjournals.org/content/12/24/7374>, doi: [10.1158/1078-0432.CCR-06-1516](https://doi.org/10.1158/1078-0432.CCR-06-1516).

780 [48] **O'Hare T**, Eide CA, Deininger MW. Bcr-Abl kinase domain mutations, drug resistance, and the road to a cure for  
781 chronic myeloid leukemia. *Blood*. 2007; 110(7):2242–2249.

782 [49] **O'Hare T**. Combined Abl Inhibitor Therapy for Minimizing Drug Resistance in Chronic Myeloid Leukemia: Src/Abl  
783 Inhibitors Are Compatible with Imatinib. *Clin Cancer Res*. 2005 Oct; 11(19):6987–6993. doi: [10.1158/1078-0432.CCR-05-0622](https://doi.org/10.1158/1078-0432.CCR-05-0622).

785 [50] **Shan Y**, Seeliger MA, Eastwood MP, Frank F, Xu H, Jensen MØ, Dror RO, Kuriyan J, Shaw DE. A Conserved Protonation-  
786 Dependent Switch Controls Drug Binding in the Abl Kinase. *Proc Natl Acad Sci.* 2009; 106(1):139–144.

787 [51] **Demerdash O**, Yap EH, Head-Gordon T. Advanced Potential Energy Surfaces for Condensed Phase Simulation. *Annu  
788 Rev Phys Chem.* 2014 Apr; 65(1):149–174. doi: 10.1146/annurev-physchem-040412-110040.

789 [52] **Jiao D**, Golubkov PA, Darden TA, Ren P. Calculation of Protein-ligand Binding Free Energy by Using a Polarizable  
790 Potential. *Proc Natl Acad Sci.* 2008; 105(17):6290–6295.

791 [53] **Shirts MR**, Mobley DL, Chodera JD, Pande VS. Accurate and Efficient Corrections for Missing Dispersion Interactions  
792 in Molecular Simulations. *J Phys Chem B.* 2007 Nov; 111(45):13052–13063. doi: 10.1021/jp0735987.

793 [54] **Essmann U**, Perera L, Berkowitz ML, Darden T, Lee H, Pedersen LG. A Smooth Particle Mesh Ewald Method. *J Chem  
794 Phys.* 1995 Nov; 103(19):8577–8593. doi: 10.1063/1.470117.

795 [55] **Wennberg CL**, Murtola T, Hess B, Lindahl E. Lennard-Jones Lattice Summation in Bilayer Simulations Has Crit-  
796 ical Effects on Surface Tension and Lipid Properties. *J Chem Theory Comput.* 2013 Aug; 9(8):3527–3537. doi:  
797 10.1021/ct400140n.

798 [56] **Onufriev AV**, Alexov E. Protonation and pK Changes in Protein-ligand Binding. *Q Rev Biophys.* 2013 May; 46(02):181–  
799 209. doi: 10.1017/S0033583513000024.

800 [57] **Martin YC**. Let's Not Forget Tautomers. *J Comput Aided Mol Des.* 2009 Oct; 23(10):693–704. doi: 10.1007/s10822-  
801 009-9303-2.

802 [58] **Jensen J**. Calculating pH and Salt Dependence of Protein-Protein Binding. *Curr Pharm Biotechnol.* 2008 Apr;  
803 9(2):96–102. doi: 10.2174/138920108783955146.

804 [59] **Nagar B**, Hantschel O, Young MA, Scheffzek K, Veach D, Bornmann W, Clarkson B, Superti-Furga G, Kuriyan J. Structural  
805 Basis for the Autoinhibition of C-Abl Tyrosine Kinase. *Cell.* 2003; 112(6):859–871.

806 [60] **Lorenz S**, Deng P, Hantschel O, Superti-Furga G, Kuriyan J. Crystal Structure of an SH2-kinase Construct of C-Abl and  
807 Effect of the SH2 Domain on Kinase Activity. *Biochem J.* 2015 Jun; 468(2):283–291. doi: 10.1042/BJ20141492.

808 [61] **O'Hare T**, Shakespeare WC, Zhu X, Eide CA, Rivera VM, Wang F, Adrian LT, Zhou T, Huang WS, Xu Q, Metcalf CA, Tyner  
809 JW, Loriaux MM, Corbin AS, Wardwell S, Ning Y, Keats JA, Wang Y, Sundaramoorthi R, Thomas M, et al. AP24534, a Pan-  
810 BCR-ABL Inhibitor for Chronic Myeloid Leukemia, Potently Inhibits the T315I Mutant and Overcomes Mutation-Based  
811 Resistance. *Cancer Cell.* 2009 Nov; 16(5):401–412. doi: 10.1016/j.ccr.2009.09.028.

812 [62] **Levinson NM**, Boxer SG. Structural and Spectroscopic Analysis of the Kinase Inhibitor Bosutinib and an Isomer  
813 of Bosutinib Binding to the Abl Tyrosine Kinase Domain. *PLoS ONE.* 2012 Apr; 7(4):e29828. doi: 10.1371/journal.  
814 pone.0029828.

815 [63] **Weisberg E**, Manley PW, Breitenstein W, Brüggen J, Cowan-Jacob SW, Ray A, Huntly B, Fabbro D, Fendrich G, Hall-  
816 Meyers E, Kung AL, Mestan J, Daley GQ, Callahan L, Catley L, Cavazza C, Mohammed A, Neuberg D, Wright RD, Gilliland  
817 DG, et al. Characterization of AMN107, a Selective Inhibitor of Native and Mutant Bcr-Abl. *Cancer Cell.* 2005 Feb;  
818 7(2):129–141. doi: 10.1016/j.ccr.2005.01.007.

819 [64] **Zhou T**, Commodore L, Huang WS, Wang Y, Thomas M, Keats J, Xu Q, Rivera VM, Shakespeare WC, Clackson T, Dalgarno  
820 DC, Zhu X. Structural Mechanism of the Pan-BCR-ABL Inhibitor Ponatinib (AP24534): Lessons for Overcoming  
821 Kinase Inhibitor Resistance: Structural Mechanism of Ponatinib. *Chem Biol Drug Des.* 2011 Jan; 77(1):1–11. doi:  
822 10.1111/j.1747-0285.2010.01054.x.

823 [65] **Li H**, Robertson AD, Jensen JH. Very Fast Empirical Prediction and Rationalization of Protein pKa Values. *Proteins  
824 Struct Funct Bioinforma.* 2005 Oct; 61(4):704–721. doi: 10.1002/prot.20660.

825 [66] **Friesner RA**, Banks JL, Murphy RB, Halgren TA, Klicic JJ, Mainz DT, Repasky MP, Knoll EH, Shelley M, Perry JK, Shaw DE,  
826 Francis P, Shenkin PS. Glide: A New Approach for Rapid, Accurate Docking and Scoring. 1. Method and Assessment of  
827 Docking Accuracy. *J Med Chem.* 2004 Mar; 47(7):1739–1749. doi: 10.1021/jm0306430.

828 [67] **Park JH**, Liu Y, Lemmon MA, Radhakrishnan R. Erlotinib Binds Both Inactive and Active Conformations of the EGFR  
829 Tyrosine Kinase Domain. *Biochem J.* 2012 Dec; 448(3):417–423. doi: 10.1042/BJ20121513.

830 [68] **Yosaatmadja Y**, Squire CJ. 1.85 Angstrom Structure of EGFR Kinase Domain with Gefitinib. . 2014 Nov; doi:  
831 10.2210/pdb4wkq/pdb.

832 [69] **Shelley JC**, Cholleti A, Frye LL, Greenwood JR, Timlin MR, Uchimaya M. Epik: A Software Program for pK a Prediction  
833 and Protonation State Generation for Drug-like Molecules. *J Comput Aided Mol Des.* 2007 Dec; 21(12):681–691. doi:  
834 10.1007/s10822-007-9133-z.

835 [70] **Berendsen HJC**, Postma JPM, van Gunsteren WF, Hermans J. Interaction Models for Water in Relation to Protein  
836 Hydration. In: Pullman B, editor. *Intermolecular Forces*, vol. 14 Dordrecht: Springer Netherlands; 1981.p. 331–342. doi:  
837 10.1007/978-94-015-7658-1\_21.

838 [71] **Shivakumar D**, Williams J, Wu Y, Damm W, Shelley J, Sherman W. Prediction of Absolute Solvation Free Energies  
839 Using Molecular Dynamics Free Energy Perturbation and the OPLS Force Field. *J Chem Theory Comput.* 2010 May;  
840 6(5):1509–1519. doi: 10.1021/ct900587b.

841 [72] **Pearlman DA**. A Comparison of Alternative Approaches to Free Energy Calculations. *J Phys Chem.* 1994 Feb;  
842 98(5):1487–1493. doi: 10.1021/j100056a020.

843 [73] **Rocklin GJ**, Mobley DL, Dill KA, Hünenberger PH. Calculating the Binding Free Energies of Charged Species Based  
844 on Explicit-Solvent Simulations Employing Lattice-Sum Methods: An Accurate Correction Scheme for Electrostatic  
845 Finite-Size Effects. *J Chem Phys.* 2013 Nov; 139(18):184103. doi: 10.1063/1.4826261.

846 [74] **Feller SE**, Zhang Y, Pastor RW, Brooks BR. Constant pressure molecular dynamics simulation: The Langevin piston  
847 method. *The Journal of Chemical Physics.* 1995; 103(11):4613–4621. <https://doi.org/10.1063/1.470648>, doi:  
848 10.1063/1.470648.

849 [75] **Essmann U**, Perera L, Berkowitz ML, Darden T, Lee H, Pedersen LG. A smooth particle mesh Ewald method. *The  
850 Journal of Chemical Physics.* 1995; 103(19):8577–8593. <https://doi.org/10.1063/1.470117>, doi: 10.1063/1.470117.

851 [76] **Martyna GJ**, Tobias DJ, Klein ML. Constant pressure molecular dynamics algorithms. *The Journal of Chemical Physics.*  
852 1994; 101(5):4177–4189. <https://doi.org/10.1063/1.467468>, doi: 10.1063/1.467468.

853 [77] **Tuckerman M**, Berne BJ, Martyna GJ. Reversible multiple time scale molecular dynamics. *The Journal of Chemical Physics.*  
854 1992; 97(3):1990–2001. <https://doi.org/10.1063/1.463137>, doi: 10.1063/1.463137.

855 [78] **Hopkins CW**, Le Grand S, Walker RC, Roitberg AE. Long-Time-Step Molecular Dynamics through Hydrogen Mass  
856 Repartitioning. *Journal of Chemical Theory and Computation.* 2015; 11(4):1864–1874. <http://dx.doi.org/10.1021/ct5010406>, doi: 10.1021/ct5010406, pMID: 26574392.

858 [79] **Wang L**, Berne BJ, Friesner RA. On Achieving High Accuracy and Reliability in the Calculation of Relative Protein-Ligand  
859 Binding Affinities. *Proc Natl Acad Sci.* 2012 Feb; 109(6):1937–1942. doi: 10.1073/pnas.1114017109.

860 [80] **Bennett CH**. Efficient Estimation of Free Energy Differences from Monte Carlo Data. *J Comput Phys.* 1976; 22:245–  
861 268.

862 [81] **Shirts MR**, Bair E, Hooker G, Pande VS. Equilibrium Free Energies from Nonequilibrium Measurements Using  
863 Maximum-Likelihood Methods. *Phys Rev Lett.* 2003 Oct; 91(14). doi: 10.1103/PhysRevLett.91.140601.

864 [82] **Price DJ**, Jorgensen WL. Computational Binding Studies of Human Pp60c-Src SH2 Domain with a Series of Nonpeptide,  
865 Phosphophenyl-Containing Ligands. *Bioorg Med Chem Lett.* 2000 Sep; 10(18):2067–2070. doi: 10.1016/S0960-  
866 894X(00)00401-7.

867 [83] **Luccarelli J**, Michel J, Tirado-Rives J, Jorgensen WL. Effects of Water Placement on Predictions of Binding Affinities for  
868 P38 $\alpha$  MAP Kinase Inhibitors. *J Chem Theory Comput.* 2010 Dec; 6(12):3850–3856. doi: 10.1021/ct100504h.

869 [84] **Michel J**, Verdonk ML, Essex JW. Protein-Ligand Binding Affinity Predictions by Implicit Solvent Simulations: A Tool for  
870 Lead Optimization? *J Med Chem.* 2006 Dec; 49(25):7427–7439. doi: 10.1021/jm061021s.

871 [85] **Barouch-Bentov R**, Sauer K. Mechanisms of drug resistance in kinases. *Expert opinion on investigational drugs.*  
872 2011 Feb; 20(2):153–208.

873 [86] **McDermott U**, Sharma SV, Dowell L, Greninger P, Montagut C, Lamb J, Archibald H, Raudales R, Tam A, Lee D,  
874 Rothenberg SM, Supko JG, Sordella R, Ulkus LE, Iafrate AJ, Maheswaran S, Njauw CN, Tsao H, Drew L, Hanke JH,  
875 et al. Identification of genotype-correlated sensitivity to selective kinase inhibitors by using high-throughput tumor  
876 cell line profiling. *Proceedings of the National Academy of Sciences of the United States of America.* 2007 Dec;  
877 104(50):19936–19941.

878 [87] **Salvatier J**, Wiecki TV, Fonnesbeck C. Probabilistic programming in Python using PyMC3. *PeerJ Computer Science.*  
879 2016 Apr; 2:e55. <https://doi.org/10.7717/peerj-cs.55>, doi: 10.7717/peerj-cs.55.

880 [88] **Gruber FX**, Lundán T, Goll R, Silye A, Mikkola I, Rekvig OP, Knuutila S, Remes K, Gedde-Dahl T, Porkka K, Hjorth-Hansen  
881 H. BCR-ABL Isoforms Associated with Intrinsic or Acquired Resistance to Imatinib: More Heterogeneous than Just  
882 ABL Kinase Domain Point Mutations? *Med Oncol*. 2012 Mar; 29(1):219–226. doi: 10.1007/s12032-010-9781-z.

883 [89] **Redaelli S**, Mologni L, Rostagno R, Piazza R, Magistroni V, Ceccon M, Viltadi M, Flynn D, Passerini CG. Three novel  
884 patient-derived BCR/ABL mutants show different sensitivity to second and third generation tyrosine kinase inhibitors.  
885 *American Journal of Hematology*. 2012; 87(11):E125–E128. <https://onlinelibrary.wiley.com/doi/abs/10.1002/ajh.23338>,  
886 doi: 10.1002/ajh.23338.

887 [90] **Cortes JE**, Kantarjian H, Shah NP, Bixby D, Mauro MJ, Flinn I, O'Hare T, Hu S, Narasimhan NI, Rivera VM, Clackson  
888 T, Turner CD, Haluska FG, Druker BJ, Deininger MWN, Talpaz M. Ponatinib in Refractory Philadelphia Chromo-  
889 some-Positive Leukemias. *N Engl J Med*. 2012 Nov; 367(22):2075–2088. doi: 10.1056/NEJMoa1205127.

890 [91] **Branford S**. High Frequency of Point Mutations Clustered within the Adenosine Triphosphate-Binding Region of  
891 BCR/ABL in Patients with Chronic Myeloid Leukemia or Ph-Positive Acute Lymphoblastic Leukemia Who Develop  
892 Imatinib (ST1571) Resistance. *Blood*. 2002 May; 99(9):3472–3475. doi: 10.1182/blood.V99.9.3472.

893 [92] **Press RD**, Willis SG, Laudadio J, Mauro MJ, Deininger MWN. Determining the rise in BCR-ABL RNA that optimally  
894 predicts a kinase domain mutation in patients with chronic myeloid leukemia on imatinib. *Blood*. 2009; 114(13):2598–  
895 2605. <http://www.bloodjournal.org/content/114/13/2598>, doi: 10.1182/blood-2008-08-173674.

896 **Supplementary Information**

897 **TITLE**

898 Predicting resistance of clinical Abl mutations to targeted kinase inhibitors using alchemical free-energy  
899 calculations

900 **AUTHORS**

901 Kevin Hauser<sup>1</sup>, Christopher Negron<sup>1</sup>, Steven K. Albanese<sup>3,4</sup>, Soumya Ray<sup>1</sup>, Thomas Steinbrecher<sup>4</sup>, Robert  
902 Abel<sup>1</sup>, John D. Chodera<sup>3</sup>, Lingle Wang<sup>1,\*</sup>

903 **AFFILIATIONS**

904 <sup>1</sup>Schrödinger, New York, NY 10036. <sup>2</sup>Gerstner Sloan Kettering Graduate School, Memorial Sloan Kettering  
905 Cancer Center, New York, NY 10065. <sup>3</sup>Computational and Systems Biology Program, Sloan Kettering Institute,  
906 Memorial Sloan Kettering Cancer Center, New York, NY 10065. <sup>4</sup>Schrödinger, GmbH, Q7 23, 68161 Mannheim,  
907 Germany.

908 **CORRESPONDING AUTHOR**

909 \*Corresponding Author: *lingle.wang@schrodinger.com* (LW)

910 **CONTENTS**

- 911 • **Figure S1:** Comparison of 31 mutations for which phosphorylated and non-phosphorylated  $\Delta K_d$ s were  
912 available.
- 913 • **Figure S2:** Truth tables with varying classification cutoffs for each TKI.
- 914 • **Figure S3:** ROC curves for non-scaled and scaled FEP+, non-scaled and scaled Prime, a consensus  
915 model and a naïve model.
- 916 • **Table S1:** IC<sub>50</sub> experiment-derived reference  $\Delta\Delta G$  data.
- 917 • **Table S2:** Axitinib: experimental IC<sub>50</sub> data and alchemical free-energy  $\Delta\Delta G$ s.
- 918 • **Table S3:** Bosutinib: experimental IC<sub>50</sub> data and alchemical free-energy  $\Delta\Delta G$ s.
- 919 • **Table S4:** Dasatinib: experimental IC<sub>50</sub> data and alchemical free-energy  $\Delta\Delta G$ s.
- 920 • **Table S5:** Imatinib: experimental IC<sub>50</sub> data and alchemical free-energy  $\Delta\Delta G$ s.
- 921 • **Table S6:** Nilotinib: experimental IC<sub>50</sub> data and alchemical free-energy  $\Delta\Delta G$ s.
- 922 • **Table S7:** Ponatinib: experimental IC<sub>50</sub> data and alchemical free-energy  $\Delta\Delta G$ s.
- 923 • **Table S8:** Summary of statistics of scaled predictions, a naïve model, and a consensus model.
- 924 • **Table S9:** Summary of the preparation of the 6 Abl:TKI co-crystal structure complexes.

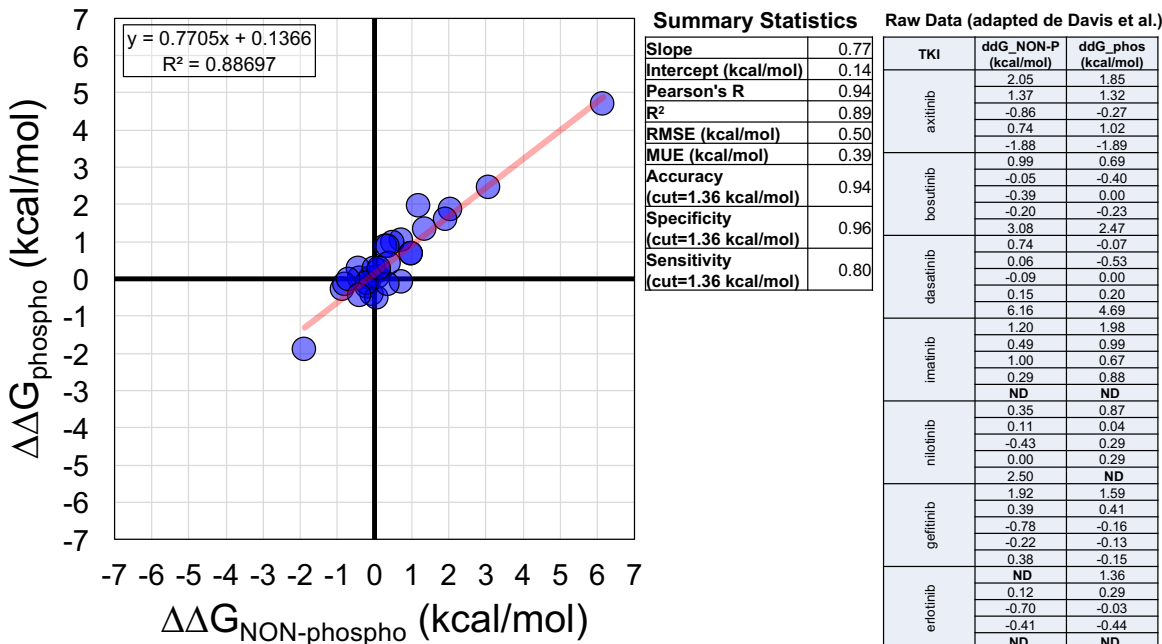


**Figure S1. Comparison of 31 mutations for which phosphorylated and non-phosphorylated  $\Delta K_d$ s were available.**  
 Scatter plot compares  $\Delta\Delta G$ s (derived from the  $\Delta K_d$ s) and contains the best-fit line with slope 0.77 and intercept 0.14. Summary statistics for this comparison are also shown. The raw  $\Delta\Delta G$ s used for this comparison were adapted from [46]; kino-bead data for ponatinib was not available.

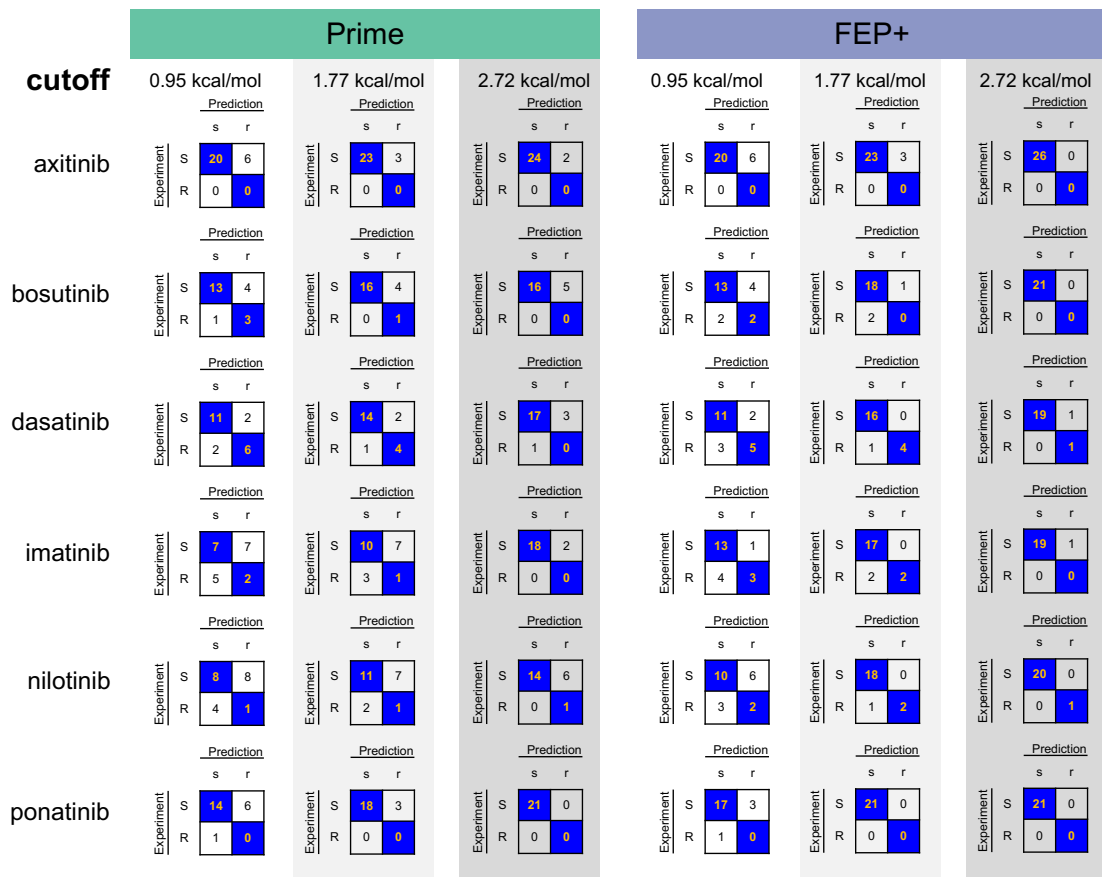


**Figure S2. TKI-by-TKI truth tables with increasingly large classification cutoffs.** Truth tables for the six TKIs (axitinib, bosutinib, dasatinib, imatinib, nilotinib, and ponatinib) using Prime (left, green) and FEP+ (right, blue) with classification cutoff values defining whether mutations are susceptible (S, experiment; s, prediction) or resistant (R, experiment; r, prediction). A mutation is susceptible if  $\Delta\Delta G \leq \text{cutoff}$  or resistant if  $\Delta\Delta G > \text{cutoff}$ .

Preprint at <https://doi.org/10.1101/239012>; this version posted March 30, 2018

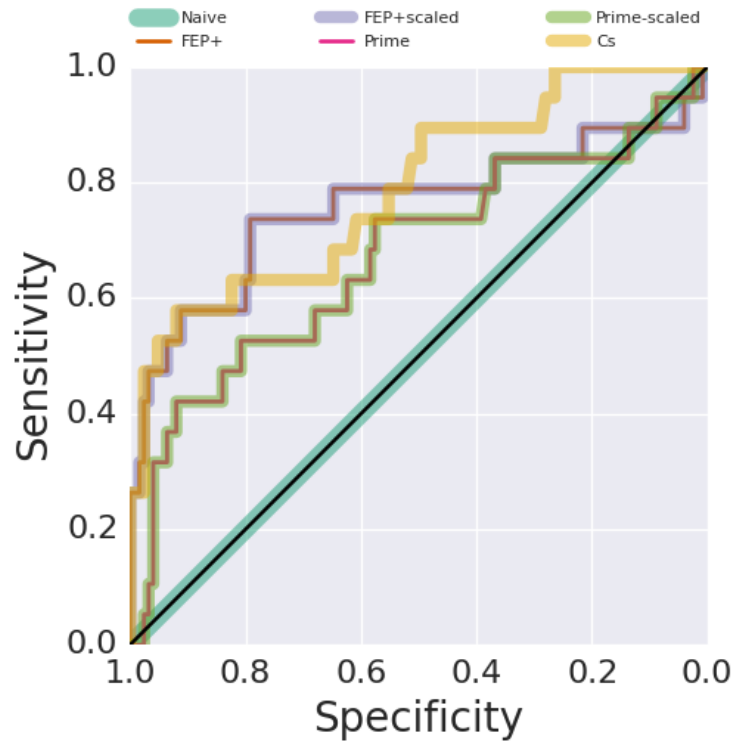


**Figure S3. ROC curves for non-scaled and scaled FEP+, non-scaled and scaled Prime, a consensus model and a naïve model.** ROC-AUC for scaled and non-scaled FEP+ was  $0.75_{0.61}^{0.90}$  (n=144); ROC-AUC for scaled and non-scaled Prime was  $0.66_{0.52}^{0.81}$  (n=144); ROC-AUCs for the naïve model and consensus model were  $0.50_{0.50}^{0.50}$  (n=144) and  $0.78_{0.67}^{0.90}$  (n=144) respectively. Optimal scaling factors ( $\alpha=0.34$  for FEP+;  $\alpha=0.23$  for Prime) obtained using linear regression ( $m=142$ ) were applied to the full dataset (n=144), which was used in this ROC analysis. ROC-AUC interpretations: [0.50,0.60], failure; [0.60,0.70], poor; [0.70,0.80], fair; [0.80,0.90], good; [0.90,1.00], excellent.

**Table S1.**  $\Delta\Delta G$  data derived from publicly available  $\Delta\text{pIC}_{50}$  measurements and sources of mutation clinical-observation

Mutation	axitinib	bosutinib	dasatinib	imatinib	nilotinib	ponatinib	gefitinib	erlotinib	Source of Clinical-Observation
	$\Delta\Delta G$ (kcal/mol)								
M244V	-0.11	0.43	0.00	0.21	-0.13	0.00	nd	nd	A
L248R	0.31	1.50	0.65	2.33	2.15	0.58	nd	nd	B
L248V	0.32	0.56	0.55	0.64	0.33	0.17	nd	nd	A,C
G250E	0.27	0.11	0.41	1.01	0.60	0.30	nd	nd	A,C,D
Q252H	0.20	nd	nd	nd	nd	nd	-0.44	-0.13	A
Y253F	0.26	-0.34	0.24	1.90	1.48	0.30	-0.17	0.00	C
Y253H	0.03	nd	A,C,D						
E255K	0.26	0.56	0.90	1.50	1.27	0.41	-0.11	-0.11	A,C,D
E255V	0.30	0.66	1.02	2.22	2.36	1.00	nd	nd	A,C
D276G	0.18	nd	C						
E279K	-0.03	nd	C						
E292L	0.03	nd	E						
V299L	-0.88	1.70	1.24	0.23	0.28	0.17	nd	nd	C
T315A	-0.45	0.32	2.02	0.51	0.72	0.17	nd	nd	C
T315I	-1.27	2.45	5.08	2.32	3.75	0.41	nd	-0.15	C,D
T315V	-1.73	nd	B						
F317C	nd	0.50	1.86	0.28	0.04	0.00	nd	nd	A <sup>g</sup>
F317I	nd	0.71	1.79	0.17	0.30	0.51	1.35	1.58	C
F317L	0.23	0.09	0.96	0.72	0.20	0.17	0.29	0.40	C,D
F317R	0.27	nd	B						
F317V	0.28	1.72	2.36	0.97	0.33	0.72	nd	nd	C
M343T	0.21	nd	F <sup>h</sup>						
M351T	-0.24	0.19	0.00	0.42	0.00	0.17	0.05	-0.08	A,C,D
E355A	nd	0.02	0.24	0.47	0.11	0.51	nd	nd	C
F359C	nd	-0.01	0.00	0.77	0.68	0.41	nd	nd	C
F359I	0.10	0.04	0.24	0.28	0.86	0.77	nd	nd	A
F359V	0.07	-0.11	0.00	0.32	0.60	0.17	nd	nd	A,C
L384M	0.06	nd	F <sup>i</sup>						
H396R	0.25	-0.10	0.00	0.40	0.25	0.17	nd	nd	A <sup>j</sup>
F486S	0.05	nd	A <sup>k</sup>						
E459K	nd	0.35	0.41	0.66	0.55	0.30	nd	nd	C

A: Gruber et al. ([88])

B: Redaelli et al. ([89])

C: Cortes et al. ([90])

D: Branford et al. ([91])

E: Press et al. ([92])

F: Shah et al. ([3])

<sup>g</sup>: F317C observed with Δ27-183

<sup>h</sup>: M343T observed as compound mutation with H396R

<sup>i</sup>: L384M observed as compound mutation with M343T

<sup>j</sup>: H396R observed as compound mutation with F486S

<sup>k</sup>: F486S observed as compound mutation with H396R

**Table S2. Axitinib: experimental  $IC_{50}$  values and alchemical free-energy  $\Delta\Delta G$ s for each mutation.**

	Expt. $IC_{50}$	Expt. $\Delta\Delta G$	Prime $\Delta\Delta G$	FEP+ $Run_1$ $\Delta\Delta G$	FEP+ $Run_1$ BAR err	FEP+ $Run_2$ $\Delta\Delta G$	FEP+ $Run_2$ BAR err	FEP+ $Run_3$ $\Delta\Delta G$	FEP+ $Run_3$ BAR err	$\Delta\Delta G_{Av}$	SE
	(nM)	(kcal/mol)	(kcal/mol)	(kcal/mol)	(kcal/mol)	(kcal/mol)	(kcal/mol)	(kcal/mol)	(kcal/mol)	(kcal/mol)	
wild-type	823										
M244V	690	-0.11	-0.10	-0.40	0.41	-0.35	0.41	-0.43	0.41	-0.39	0.02
L248R	1393	0.31	-0.06	2.13	0.43	2.42	0.45	2.46	0.43	2.34	0.10
L248V	1399	0.32	6.02	-1.32	0.41	-1.04	0.42	-1.22	0.42	-1.19	0.08
G250E	1295	0.27	0.31	-0.35	0.41	-0.71	0.41	-0.74	0.41	-0.60	0.13
Q252H	1155	0.20	-0.18	0.07	0.43	0.30	0.42	0.29	0.43	0.22	0.08
Y253F	1275	0.26	1.11	0.77	0.43	0.23	0.43	1.15	0.45	0.72	0.27
Y253H	867	0.03	4.65	1.14	0.47	0.38	0.49	-0.19	0.45	0.44	0.39
E255K	1282	0.26	0.12	1.30	0.44	0.63	0.43	1.10	0.44	1.01	0.20
E255V	1350	0.30	-0.29	0.98	0.42	1.04	0.42	1.26	0.43	1.09	0.09
D276G	1105	0.18	-0.01	0.03	0.42	0.64	0.42	0.44	0.43	0.37	0.18
E279K	778	-0.03	-0.15	0.06	0.42	-0.22	0.43	1.27	0.43	0.37	0.46
E292L	863	0.03	-0.00	0.53	0.43	0.35	0.42	0.31	0.42	0.40	0.07
V299L	188	-0.88	-5.00	-1.08	0.42	-1.39	0.42	-1.37	0.42	-1.28	0.10
T315A	389	-0.45	0.99	0.09	0.43	0.24	0.47	0.31	0.42	0.21	0.06
T315I	98	-1.27	-2.30	-1.26	0.42	-1.50	0.45	-1.39	0.43	-1.38	0.07
T315V	45	-1.73	-1.07	-1.10	0.41	-1.32	0.42	-1.15	0.48	-1.19	0.07
F317L	1220	0.23	1.29	-0.64	0.41	-0.10	0.41	-0.38	0.41	-0.37	0.16
F317R	1286	0.27	-2.46	2.64	0.46	2.27	0.51	1.38	0.47	2.10	0.37
F317V	1320	0.28	2.29	0.45	0.42	0.70	0.42	0.75	0.42	0.63	0.09
M343T	1175	0.21	-0.04	-0.26	0.54	-0.50	0.53	-0.58	0.50	-0.45	0.10
M351T	553	-0.24	-0.07	-0.25	0.41	-0.03	0.41	0.37	0.41	0.03	0.18
F359I	975	0.10	-0.04	1.89	0.41	1.60	0.42	1.78	0.41	1.76	0.08
F359V	933	0.07	-0.07	2.68	0.42	1.55	0.42	1.64	0.41	1.96	0.36
L384M	916	0.06	-0.01	-0.07	0.41	0.27	0.41	0.23	0.41	0.14	0.11
H396R	1247	0.25	-0.02	0.36	0.42	1.23	0.41	0.65	0.42	0.75	0.26
F486S	897	0.05	-0.09	0.65	0.47	1.14	0.46	0.44	0.48	0.74	0.21

**BAR err:** Bennett Acceptance Ratio error.

**$\Delta\Delta G_{Av}$ :** Average of three independent FEP+ runs.

**SE:** Standard Error between three independent FEP+ runs.

**Table S3. Bosutinib: experimental IC<sub>50</sub> values and alchemical free-energy ΔΔGs for each mutation.**

	Expt. IC <sub>50</sub> (nM)	Expt. ΔΔG (kcal/mol)	Prime ΔΔG (kcal/mol)	FEP+ <sub>Run1</sub> ΔΔG (kcal/mol)	FEP+ <sub>Run1</sub> BAR err (kcal/mol)	FEP+ <sub>Run2</sub> ΔΔG (kcal/mol)	FEP+ <sub>Run2</sub> BAR err (kcal/mol)	FEP+ <sub>Run3</sub> ΔΔG (kcal/mol)	FEP+ <sub>Run3</sub> BAR err (kcal/mol)	ΔΔG <sub>Av</sub> (kcal/mol)	SE (kcal/mol)
wild-type	71										
M244V	147	0.43	0.02	-0.28	0.41	-0.11	0.41	-0.08	0.41	-0.16	0.06
L248R	874	1.50	3.67	1.00	0.43	1.63	0.43	1.33	0.43	1.32	0.18
L248V	182	0.56	5.77	0.37	0.41	0.72	0.42	0.38	0.42	0.49	0.12
G250E	85	0.11	-0.30	0.28	0.43	0.63	0.43	-1.07	0.43	-0.05	0.52
Y253F	40	-0.34	-0.03	0.21	0.45	0.02	0.43	0.95	0.43	0.39	0.28
E255K	181	0.56	0.49	-1.01	0.43	-1.30	0.43	-1.01	0.43	-1.11	0.10
E255V	214	0.66	0.11	-0.47	0.42	-0.51	0.43	-0.91	0.43	-0.63	0.14
V299L	1228	1.70	-0.85	0.97	0.43	0.90	0.42	0.85	0.42	0.91	0.03
T315A	122	0.32	1.00	-1.61	0.41	-1.61	0.41	-1.97	0.41	-1.73	0.12
T315I	4338	2.45	3.75	-2.32	0.43	-2.21	0.42	-1.26	0.42	-1.93	0.34
F317C	165	0.50	4.83	1.04	0.41	1.27	0.41	1.22	0.42	1.18	0.07
F317I	232	0.71	1.61	0.16	0.41	0.07	0.42	0.02	0.41	0.08	0.04
F317L	82	0.09	-0.71	0.05	0.41	0.47	0.41	0.24	0.41	0.25	0.12
F317V	1280	1.72	4.12	1.98	0.42	1.50	0.42	2.25	0.42	1.91	0.22
M351T	97	0.19	0.02	0.36	0.42	0.82	0.41	0.71	0.41	0.63	0.14
E355A	74	0.02	0.13	-0.20	0.44	0.13	0.43	0.27	0.43	0.07	0.14
F359C	70	-0.01	-0.09	3.02	0.42	2.51	0.42	1.97	0.43	2.50	0.30
F359I	76	0.04	-0.06	0.66	0.41	1.74	0.41	1.43	0.42	1.28	0.32
F359V	59	-0.11	-0.06	0.98	0.43	1.69	0.41	1.91	0.42	1.53	0.28
H396R	60	-0.10	-1.07	0.62	0.42	-0.07	0.42	-0.93	0.43	-0.13	0.45
E459K	127	0.35	0.26	-0.69	0.42	0.23	0.42	-0.54	0.42	-0.33	0.28

**BAR err:** Bennett Acceptance Ratio error.

**ΔΔG<sub>Av</sub>:** Average of three independent FEP+ runs.

**SE:** Standard Error between three independent FEP+ runs.

**Table S4. Dasatinib: experimental IC<sub>50</sub> values and alchemical free-energy ΔΔGs for each mutation.**

	Expt. IC <sub>50</sub> (nM)	Expt. ΔΔG (kcal/mol)	Prime ΔΔG (kcal/mol)	FEP+ Run1 ΔΔG (kcal/mol)	FEP+ Run1 BAR err (kcal/mol)	FEP+ Run2 ΔΔG (kcal/mol)	FEP+ Run2 BAR err (kcal/mol)	FEP+ Run3 ΔΔG (kcal/mol)	FEP+ Run3 BAR err (kcal/mol)	ΔΔG <sub>Av</sub> (kcal/mol)	SE (kcal/mol)
wild-type	2										
M244V	2	0.00	-0.10	0.05	0.41	-0.37	0.41	-0.43	0.41	-0.25	0.15
L248R	6	0.65	-2.13	1.40	0.42	1.50	0.43	1.51	0.42	1.47	0.04
L248V	5	0.55	2.60	0.58	0.42	0.70	0.41	0.79	0.41	0.69	0.06
G250E	4	0.41	-0.00	-0.54	0.43	-0.31	0.43	0.01	0.44	-0.28	0.16
Y253F	3	0.24	0.00	-0.21	0.43	-0.24	0.43	-0.03	0.44	-0.16	0.07
E255K	9	0.90	-0.08	-0.30	0.43	-0.17	0.44	-1.05	0.43	-0.51	0.27
E255V	11	1.02	-0.08	0.06	0.42	-0.80	0.42	-0.12	0.42	-0.29	0.26
V299L	16	1.24	0.01	0.83	0.41	0.36	0.42	0.77	0.42	0.65	0.15
T315A	59	2.02	5.09	-1.74	0.41	-1.65	0.41	-1.23	0.41	-1.54	0.16
T315I	10000	5.08	-2.69	5.63	0.43	4.69	0.44	5.50	0.43	5.27	0.29
F317C	45	1.86	4.72	2.63	0.42	2.32	0.42	2.62	0.41	2.52	0.10
F317I	40	1.79	2.38	1.94	0.41	2.04	0.41	1.94	0.41	1.97	0.03
F317L	10	0.96	1.22	1.26	0.41	1.42	0.41	1.08	0.41	1.25	0.10
F317V	104	2.36	4.08	3.12	0.42	2.84	0.42	2.68	0.42	2.88	0.13
M351T	2	0.00	0.04	0.04	0.41	0.14	0.41	0.00	0.42	0.06	0.04
E355A	3	0.24	0.00	-0.24	0.43	-0.87	0.45	-1.25	0.44	-0.79	0.29
F359C	2	0.00	-0.03	1.24	0.42	0.68	0.41	1.38	0.42	1.10	0.21
F359I	3	0.24	-0.02	-0.50	0.42	-0.33	0.42	-1.14	0.42	-0.66	0.25
F359V	2	0.00	-0.03	-0.87	0.41	0.57	0.42	-0.62	0.41	-0.31	0.44
H396R	2	0.00	2.53	-0.76	0.43	-0.09	0.43	-0.06	0.43	-0.30	0.23
E459K	4	0.41	0.00	-0.68	0.42	-0.17	0.42	-0.07	0.41	-0.31	0.19

T315I was beyond the concentration limit of the assay (10,000 nM).

**BAR err:** Bennett Acceptance Ratio error.

**ΔΔG<sub>Av</sub>:** Average of three independent FEP+ runs.

**SE:** Standard Error between three independent FEP+ runs.

**Table S5. Imatinib: experimental IC<sub>50</sub> values and alchemical free-energy ΔΔGs for each mutation.**

	Expt. IC <sub>50</sub> (nM)	Expt. ΔΔG (kcal/mol)	Prime ΔΔG (kcal/mol)	FEP+ Run1 ΔΔG (kcal/mol)	FEP+ Run1 BAR err (kcal/mol)	FEP+ Run2 ΔΔG (kcal/mol)	FEP+ Run2 BAR err (kcal/mol)	FEP+ Run3 ΔΔG (kcal/mol)	FEP+ Run3 BAR err (kcal/mol)	ΔΔG <sub>Av</sub> (kcal/mol)	SE (kcal/mol)
wild-type 201											
M244V	287	0.21	-0.08	0.15	0.41	0.43	0.41	0.17	0.41	0.25	0.09
L248R	10000	2.33	1.92	1.92	0.43	2.52	0.44	2.34	0.43	2.26	0.18
L248V	586	0.64	1.89	-1.04	0.41	-1.02	0.42	-1.20	0.41	-1.09	0.06
G250E	1087	1.01	0.92	0.16	0.41	0.02	0.41	0.12	0.41	0.10	0.04
Y253F	4908	1.90	-0.02	0.87	0.43	0.65	0.42	1.34	0.44	0.95	0.20
E255K	2487	1.50	0.25	-0.12	0.44	1.95	0.44	-0.55	0.44	0.43	0.77
E255V	8322	2.22	0.24	-0.72	0.42	-0.02	0.42	-0.53	0.43	-0.42	0.21
V299L	295	0.23	-1.29	0.66	0.41	0.26	0.42	-0.37	0.42	0.18	0.30
T315A	476	0.51	5.10	-1.39	0.41	-1.86	0.41	-2.09	0.44	-1.78	0.21
T315I	9773	2.32	0.88	4.23	0.43	4.23	0.42	3.14	0.44	3.87	0.36
F317C	324	0.28	2.10	0.27	0.42	-0.18	0.41	0.45	0.42	0.18	0.19
F317I	266	0.17	0.94	0.59	0.41	0.66	0.41	0.48	0.41	0.58	0.05
F317L	675	0.72	0.74	0.58	0.41	0.53	0.41	0.38	0.41	0.50	0.06
F317V	1023	0.97	1.57	0.71	0.42	0.79	0.42	0.80	0.41	0.77	0.03
M351T	404	0.42	-0.02	1.72	0.41	1.03	0.42	1.20	0.42	1.32	0.21
E355A	441	0.47	0.29	0.13	0.43	0.08	0.44	0.14	0.43	0.12	0.02
F359C	728	0.77	2.43	0.88	0.42	0.47	0.41	0.33	0.42	0.56	0.17
F359I	324	0.28	1.95	-0.13	0.41	-0.87	0.41	0.08	0.41	-0.31	0.29
F359V	346	0.32	2.53	-0.66	0.41	0.02	0.41	-0.27	0.42	-0.30	0.20
H396R	395	0.40	2.76	-0.39	0.41	-0.38	0.42	-0.39	0.42	-0.39	0.00
E459K	612	0.66	0.24	-0.09	0.43	-0.09	0.42	-0.08	0.42	-0.09	0.00

T315I was beyond the concentration limit of the assay (10,000 nM).

**BAR err:** Bennett Acceptance Ratio error.

**ΔΔG<sub>Av</sub>:** Average of three independent FEP+ runs.

**SE:** Standard Error between three independent FEP+ runs.

**Table S6. Nilotinib: experimental  $IC_{50}$  values and alchemical free-energy  $\Delta\Delta G$ s for each mutation.**

	Expt. $IC_{50}$ (nM)	Expt. $\Delta\Delta G$ (kcal/mol)	Prime $\Delta\Delta G$ (kcal/mol)	FEP+ <sub>Run1</sub> $\Delta\Delta G$ (kcal/mol)	FEP+ <sub>Run1</sub> BAR err (kcal/mol)	FEP+ <sub>Run2</sub> $\Delta\Delta G$ (kcal/mol)	FEP+ <sub>Run2</sub> BAR err (kcal/mol)	FEP+ <sub>Run3</sub> $\Delta\Delta G$ (kcal/mol)	FEP+ <sub>Run3</sub> BAR err (kcal/mol)	$\Delta\Delta G_{Av}$ (kcal/mol)	SE (kcal/mol)
wild-type 15											
M244V	12	-0.13	-0.11	0.15	0.41	-0.21	0.41	0.21	0.41	0.05	0.13
L248R	549	2.15	0.48	2.05	0.43	2.12	0.47	1.93	0.43	2.03	0.06
L248V	26	0.33	3.53	-0.50	0.42	-0.39	0.41	-0.92	0.41	-0.60	0.16
G250E	41	0.60	0.05	0.06	0.41	-0.27	0.41	-0.38	0.41	-0.20	0.13
Y253F	179	1.48	-0.27	1.09	0.43	0.42	0.42	1.16	0.42	0.89	0.24
E255K	127	1.27	0.41	-2.24	0.48	-1.52	0.46	0.33	0.46	-1.14	0.77
E255V	784	2.36	-0.03	0.31	0.42	-0.25	0.43	-0.55	0.43	-0.16	0.25
V299L	24	0.28	2.94	-0.18	0.41	0.21	0.41	0.15	0.41	0.06	0.12
T315A	50	0.72	3.38	-1.33	0.41	-1.31	0.41	-1.39	0.41	-1.34	0.02
T315I	8091	3.75	4.16	4.29	0.43	5.00	0.42	4.34	0.43	4.54	0.23
F317C	16	0.04	0.90	1.34	0.41	0.88	0.41	0.60	0.41	0.94	0.22
F317I	25	0.30	-0.18	1.24	0.41	1.17	0.41	0.82	0.41	1.08	0.13
F317L	21	0.20	1.74	1.03	0.41	1.07	0.41	1.09	0.41	1.06	0.02
F317V	26	0.33	0.77	1.16	0.41	0.68	0.42	1.07	0.42	0.97	0.15
M351T	15	0.00	0.09	-0.06	0.41	-0.09	0.42	-0.46	0.42	-0.20	0.13
E355A	18	0.11	-0.06	-0.46	0.43	-1.01	0.43	-0.32	0.43	-0.60	0.21
F359C	47	0.68	3.68	1.32	0.41	1.44	0.41	1.52	0.41	1.43	0.06
F359I	64	0.86	3.70	1.05	0.41	1.13	0.41	0.74	0.41	0.97	0.12
F359V	41	0.60	3.67	1.00	0.41	1.08	0.41	1.38	0.42	1.15	0.12
H396R	23	0.25	2.58	-0.07	0.42	0.21	0.42	0.03	0.42	0.06	0.08
E459K	38	0.55	-0.00	-0.17	0.42	-0.46	0.42	-0.10	0.42	-0.24	0.11

**BAR err:** Bennett Acceptance Ratio error.

**$\Delta\Delta G_{Av}$ :** Average of three independent FEP+ runs.

**SE:** Standard Error between three independent FEP+ runs.

**Table S7. Ponatinib: experimental IC<sub>50</sub> values and alchemical free-energy ΔΔGs for each mutation.**

	Expt. IC <sub>50</sub> (nM)	Expt. ΔΔG (kcal/mol)	Prime ΔΔG (kcal/mol)	FEP+ <sub>Run1</sub> ΔΔG (kcal/mol)	FEP+ <sub>Run1</sub> BAR err (kcal/mol)	FEP+ <sub>Run2</sub> ΔΔG (kcal/mol)	FEP+ <sub>Run2</sub> BAR err (kcal/mol)	FEP+ <sub>Run3</sub> ΔΔG (kcal/mol)	FEP+ <sub>Run3</sub> BAR err (kcal/mol)	ΔΔG <sub>Av</sub> (kcal/mol)	SE (kcal/mol)
wild-type	3										
M244V	3	0.00	-0.13	0.07	0.41	-0.28	0.41	0.12	0.41	-0.03	0.13
L248R	8	0.58	2.48	1.40	0.43	0.96	0.43	1.10	0.44	1.15	0.13
L248V	4	0.17	2.48	-1.82	0.42	-1.23	0.42	-1.96	0.42	-1.67	0.22
G250E	0.021	0.30	0.17	-0.32	0.43	-0.25	0.43	-0.71	0.46	-0.43	0.14
Y253F	5	0.30	0.05	0.85	0.43	1.32	0.44	0.77	0.43	0.98	0.17
E255K	6	0.41	1.05	-0.27	0.48	-0.66	0.48	0.03	0.47	-0.30	0.20
E255V	16	1.00	-0.04	1.19	0.43	0.94	0.43	-0.41	0.43	0.57	0.50
V299L	4	0.17	-0.29	-0.56	0.41	-0.55	0.41	-1.42	0.41	-0.84	0.29
T315A	4	0.17	-0.51	-2.90	0.41	-3.15	0.41	-2.92	0.41	-2.99	0.08
T315I	6	0.41	-5.42	0.51	0.42	0.90	0.42	0.91	0.42	0.77	0.13
F317C	3	0.00	1.45	0.44	0.41	0.98	0.42	0.80	0.41	0.74	0.16
F317I	7	0.51	0.62	-0.76	0.41	-1.03	0.41	-1.02	0.41	-0.94	0.09
F317L	4	0.17	0.57	-1.08	0.41	-0.83	0.41	-0.85	0.41	-0.92	0.08
F317V	10	0.72	1.14	0.05	0.41	-0.21	0.41	0.24	0.42	0.03	0.13
M351T	4	0.17	-0.12	0.89	0.41	1.66	0.41	0.65	0.41	1.07	0.30
E355A	7	0.51	0.01	0.12	0.44	-0.52	0.44	-0.55	0.43	-0.32	0.22
F359C	6	0.41	2.12	0.25	0.42	-0.35	0.43	0.73	0.42	0.21	0.31
F359I	11	0.77	0.34	-0.66	0.41	-0.38	0.41	0.06	0.41	-0.33	0.21
F359V	4	0.17	0.74	0.11	0.41	-0.28	0.41	0.08	0.42	-0.03	0.13
H396R	4	0.17	-0.04	0.19	0.49	0.10	0.45	-1.41	0.48	-0.37	0.52
E459K	5	0.30	-0.00	-0.51	0.42	-0.78	0.42	-0.63	0.42	-0.64	0.08

**BAR err:** Bennett Acceptance Ratio error.

**ΔΔG<sub>Av</sub>:** Average of three independent FEP+ runs.

**SE:** Standard Error between three independent FEP+ runs.

**Table S8. Summary of statistics of scaled predictions, a naïve model, and a consensus model.**

Method	Scaling factor	MUE	RMSE	Accuracy	Specificity	Sensitivity
		(kcal/mol) [N=142]	(kcal/mol) [N=142]	[N=144]	[N=144]	[N=144]
Prime	1.00	1.14 <sup>1.35</sup> <sub>0.94</sub>	1.70 <sup>1.97</sup> <sub>1.40</sub>	0.73 <sup>0.80</sup> <sub>0.65</sub>	0.76 <sup>0.83</sup> <sub>0.68</sub>	0.53 <sup>0.78</sup> <sub>0.29</sub>
Prime	0.50	0.64 <sup>0.76</sup> <sub>0.53</sub>	0.91 <sup>1.06</sup> <sub>0.77</sub>	0.84 <sup>0.90</sup> <sub>0.78</sub>	0.90 <sup>0.95</sup> <sub>0.84</sub>	0.42 <sup>0.65</sup> <sub>0.20</sub>
Prime	0.33	0.53 <sup>0.62</sup> <sub>0.44</sub>	0.76 <sup>0.87</sup> <sub>0.63</sub>	0.87 <sup>0.92</sup> <sub>0.81</sub>	0.96 <sup>0.99</sup> <sub>0.92</sub>	0.26 <sup>0.47</sup> <sub>0.08</sub>
Prime	0.23	0.49 <sup>0.59</sup> <sub>0.40</sub>	0.73 <sup>0.86</sup> <sub>0.60</sub>	0.86 <sup>0.92</sup> <sub>0.81</sub>	0.99 <sup>1.00</sup> <sub>0.97</sub>	0.00 <sup>0.00</sup> <sub>0.00</sub>
FEP+	1.00	0.79 <sup>0.91</sup> <sub>0.67</sub>	1.07 <sup>1.27</sup> <sub>0.89</sub>	0.88 <sup>0.93</sup> <sub>0.81</sub>	0.94 <sup>0.98</sup> <sub>0.89</sub>	0.47 <sup>0.72</sup> <sub>0.22</sub>
FEP+	0.34	0.55 <sup>0.64</sup> <sub>0.47</sub>	0.78 <sup>0.91</sup> <sub>0.65</sub>	0.88 <sup>0.93</sup> <sub>0.83</sub>	1.00 <sup>1.00</sup> <sub>1.00</sub>	0.11 <sup>0.27</sup> <sub>0.00</sub>
Naive	—	0.57 <sup>0.69</sup> <sub>0.46</sub>	0.87 <sup>1.04</sup> <sub>0.70</sub>	0.87 <sup>0.92</sup> <sub>0.81</sub>	1.00 <sup>1.00</sup> <sub>1.00</sub>	0.00 <sup>0.00</sup> <sub>0.00</sub>
Consensus	—	0.47 <sup>0.56</sup> <sub>0.39</sub>	0.71 <sup>0.84</sup> <sub>0.59</sub>	0.87 <sup>0.92</sup> <sub>0.81</sub>	1.00 <sup>1.00</sup> <sub>1.00</sub>	0.00 <sup>0.00</sup> <sub>0.00</sub>

**Table S9. Summary of the preparation of the 6 Abl:TKI co-crystal structure complexes.**

PDB	Receptor	Ligand	Chains	Experimental structure				Prepared model used for simulations							
				# Water <sup>a</sup>	# Rec. atoms <sup>a</sup>	# Aminos, (Chain) <sup>b</sup>	Chain used	# Water	# Rec.	# Ash	# Gh				
4wa9	Abl	Axit	A, B	305	2219 (B)	276 (B)	B	131	4580	284	Ash421	0	0	46	neutral
3ue4	Abl	Bosut	A, B	152	2187 (A)	270 (A)	A	89	4581	284	Ash421	0	0	66	NBI4401
4xey	Abl	Dasat	A, B	0	2195 (A)	269 (A)	A	0	4581	284	Ash381	0	0	59	neutral
1opj	Abl	Imat	A, B	231	2336 (B)	288 (B)	B	104	4579	284	Ash381 <sup>c</sup>	0	0	69	N51,4767
3cs9	Abl	Nilot	A, B, C, D	266	2142 (A)	264 (A)	A	99	4579	284	0	0	0	61	neutral
3oxz	Abl	Ponat	A	89	2152 (A)	268 (A)	A	89	4580	284	0	0	0	67	N3,2155

<sup>a</sup>Total number of water molecules.

<sup>b</sup>Count includes N-Acetyl/N-terminal (6 atoms) and N-methylamide/C-terminal (6 atoms) capping groups.

<sup>c</sup>Original index in experimental structure was Ash440, Ash400.  
(PDB atom name), (PDB serial).